

This is a repository copy of *High-speed single-molecule tracking of CXCL13 in the B-Follicle*.

White Rose Research Online URL for this paper:
<https://eprints.whiterose.ac.uk/130321/>

Version: Accepted Version

Article:

Miller, Helen Louise, Cosgrove, Jason, Wollman, Adam orcid.org/0000-0002-5501-8131 et al. (5 more authors) (2018) High-speed single-molecule tracking of CXCL13 in the B-Follicle. *Frontiers in immunology*. 1073. ISSN 1664-3224

<https://doi.org/10.3389/fimmu.2018.01073>

Reuse

This article is distributed under the terms of the Creative Commons Attribution (CC BY) licence. This licence allows you to distribute, remix, tweak, and build upon the work, even commercially, as long as you credit the authors for the original work. More information and the full terms of the licence here:
<https://creativecommons.org/licenses/>

Takedown

If you consider content in White Rose Research Online to be in breach of UK law, please notify us by emailing eprints@whiterose.ac.uk including the URL of the record and the reason for the withdrawal request.

High-speed single-molecule tracking of CXCL13 in the B-Follicle

Helen Miller¹, Jason Cosgrove², Adam Wollman², Peter O'Toole², Mark Coles¹, Mark C. Leake^{2*}

¹University of Oxford, United Kingdom, ²University of York, United Kingdom

Submitted to Journal:

Frontiers in Immunology

Specialty Section:

Cytokines and Soluble Mediators in Immunity

Article type:

Original Research Article

Manuscript ID:

355984

Received on:

26 Jan 2018

Revised on:

28 Apr 2018

Frontiers website link:

www.frontiersin.org

Conflict of interest statement

The authors declare that the research was conducted in the absence of any commercial or financial relationships that could be construed as a potential conflict of interest

Author contribution statement

H.M. built the bespoke fluorescence microscope, overseen by M.C.L.; J.C. prepared biological samples overseen by M.C.C. H.M. and J.C. performed the imaging; H.M. analyzed the data from all experiments with input from A.W., M.C.L. H.M. ran simulations of fluorescence data on code adapted from A.W. P.O.T. oversaw FCS and FRAP microscopy. H.M., A.W. prepared the figures with input from all authors. H.M., J.C. and M.C.L. wrote the manuscript with input from all authors.

Keywords

single-molecule imaging, Chemokines, Biophysics, lymphoid tissues., Single-molecule tracking

Abstract

Word count: 295

Soluble factors are an essential means of communication between cells and their environment. However, many molecules readily interact with extracellular matrix components, giving rise to multiple modes of diffusion. The molecular quantification of diffusion in situ is thus a challenging imaging frontier, requiring very high spatial and temporal resolution. Overcoming this methodological barrier is key to understanding the precise spatial patterning of the extracellular factors that regulate immune function. To address this, we have developed a high-speed light microscopy system capable of millisecond sampling in ex vivo tissue samples and sub-millisecond sampling in controlled in vitro samples to characterize molecular diffusion in a range of complex microenvironments. We demonstrate that this method outperforms competing tools for determining molecular mobility of fluorescence correlation spectroscopy (FCS) and fluorescence recovery after photobleaching (FRAP) for evaluation of diffusion. We then apply this approach to study the chemokine CXCL13, a key determinant of lymphoid tissue architecture, and B-cell mediated immunity. Super-resolution single-molecule tracking of fluorescently labeled CCL19 and CXCL13 in collagen matrix was used to assess the heterogeneity of chemokine mobility behaviors, with results indicating an immobile fraction and a mobile fraction for both molecules, with distinct diffusion rates of $8.4 \pm 0.2 \mu\text{m}^2\text{s}^{-1}$ and $6.2 \pm 0.3 \mu\text{m}^2\text{s}^{-1}$ respectively. To better understand mobility behaviors in situ we analyzed CXCL13-AF647 diffusion in murine lymph node tissue sections and observed both an immobile fraction and a mobile fraction with a diffusion coefficient of $6.6 \pm 0.4 \mu\text{m}^2\text{s}^{-1}$, suggesting that mobility within the follicle is also multimodal. In quantitatively studying mobility behaviors at the molecular level, we have obtained an increased understanding of CXCL13 bioavailability within the follicle. Our high-speed single-molecule tracking approach affords a novel perspective from which to understand the mobility of soluble factors relevant to the immune system.

Funding statement

Supported by the Biological Physical Sciences Institute (BPSI), MRC grants MR/ K01580X/ 1 (P.O.T. and M.C.L.), MC_PC_15073 (Z.Z., M.C.C. and M.C.L.) and BBSRC grant BB/ N006453/ 1 (A.J.M.W. and M.C.L.). J.C. is supported by a studentship from the Wellcome Trust 4-year PhD programme (WT095024MA): Combating Infectious Disease: Computational Approaches in Translation Science.

Ethics statements

(Authors are required to state the ethical considerations of their study in the manuscript, including for cases where the study was exempt from ethical approval procedures)

Does the study presented in the manuscript involve human or animal subjects: Yes

Please provide the complete ethics statement for your manuscript. Note that the statement will be directly added to the manuscript file for peer-review, and should include the following information:

- Full name of the ethics committee that approved the study
- Consent procedure used for human participants or for animal owners
- Any additional considerations of the study in cases where vulnerable populations were involved, for example minors, persons with disabilities or endangered animal species

As per the Frontiers authors guidelines, you are required to use the following format for statements involving human subjects: This study was carried out in accordance with the recommendations of [name of guidelines], [name of committee]. The protocol was approved by the [name of committee]. All subjects gave written informed consent in accordance with the Declaration of Helsinki.

For statements involving animal subjects, please use:

This study was carried out in accordance with the recommendations of 'name of guidelines, name of committee'. The protocol was approved by the 'name of committee'.

If the study was exempt from one or more of the above requirements, please provide a statement with the reason for the exemption(s).

Ensure that your statement is phrased in a complete way, with clear and concise sentences.

All experiments conformed to the ethical principles and guidelines approved by the University of York Institutional and Animal Care Use Committee.

In review

1 **High-speed single-molecule tracking of CXCL13 in the B-**
2 **Follicle**

3
4
5 Helen Miller^{1,6,+}, Jason Cosgrove^{2,3,4+}, Adam J. M. Wollman^{1,3}, Emily Taylor^{2,3},
6 Zhaoukun Zhou^{1,3}, Peter J. O' Toole^{3,5}, Mark C. Coles^{2,3,7,*} and Mark C. Leake^{1,3,*}

7
8 ¹Department of Physics

9 ²Centre of Immunology and Infection

10 ³Department of Biology

11 ⁴Department of Electronics

12 ⁵Bioscience Technology Facility

13 University of York, YO10 5DD, UK.

14 ⁶Clarendon Laboratory, Department of Physics, University of Oxford, OX1 3PU, UK.

15 ⁷Kennedy Institute of Rheumatology, University of Oxford, OX3 7FY, UK.

16
17 + Co-first authors

18 * Correspondence should be addressed to M.C.L: mark.leake@york.ac.uk and

19 M.C.C: mark.coles@kennedy.ox.ac.uk

20
21
22
23
24
25
26
27
28
29
30
31
32
33
34
35
36
37
38
39
40
41
42
43
44
45
46
47
48
49

In review

50 **Abstract**

51 Soluble factors are an essential means of communication between cells and their
52 environment. However, many molecules readily interact with extracellular matrix
53 components, giving rise to multiple modes of diffusion. The molecular quantification
54 of diffusion *in situ* is thus a challenging imaging frontier, requiring very high spatial
55 and temporal resolution. Overcoming this methodological barrier is key to
56 understanding the precise spatial patterning of the extracellular factors that regulate
57 immune function. To address this, we have developed a high-speed light microscopy
58 system capable of millisecond sampling in *ex vivo* tissue samples and sub-millisecond
59 sampling in controlled *in vitro* samples to characterize molecular diffusion in a range
60 of complex microenvironments. We demonstrate that this method outperforms
61 competing tools for determining molecular mobility of fluorescence correlation
62 spectroscopy (FCS) and fluorescence recovery after photobleaching (FRAP) for
63 evaluation of diffusion. We then apply this approach to study the chemokine
64 CXCL13, a key determinant of lymphoid tissue architecture, and B-cell mediated
65 immunity. Super-resolution single-molecule tracking of fluorescently labeled CCL19
66 and CXCL13 in collagen matrix was used to assess the heterogeneity of chemokine
67 mobility behaviors, with results indicating an immobile fraction and a mobile fraction
68 for both molecules, with distinct diffusion rates of $8.4 \pm 0.2 \mu\text{m}^2\text{s}^{-1}$ and
69 $6.2 \pm 0.3 \mu\text{m}^2\text{s}^{-1}$ respectively. To better understand mobility behaviors *in situ* we
70 analyzed CXCL13-AF647 diffusion in murine lymph node tissue sections and
71 observed both an immobile fraction and a mobile fraction with a diffusion coefficient
72 of $6.6 \pm 0.4 \mu\text{m}^2\text{s}^{-1}$, suggesting that mobility within the follicle is also multimodal. In
73 quantitatively studying mobility behaviors at the molecular level, we have obtained an
74 increased understanding of CXCL13 bioavailability within the follicle. Our high-
75 speed single-molecule tracking approach affords a novel perspective from which to
76 understand the mobility of soluble factors relevant to the immune system.

77

78 **Keywords**

79 Single-molecule imaging, single-molecule tracking, chemokines, biophysics,
80 lymphoid tissues.

81

82 **Introduction**

83 Within the immune system, soluble factors such as chemokines, cytokines, and
84 growth factors drive graded responses to extracellular signals, regulating processes
85 including immune cell recruitment at sites of infection (Kienle and Lämmermann,
86 2016), lymphoid tissue formation (Buckley et al., 2015; Drayton et al., 2006), and the
87 maturation of adaptive immune responses (Pereira et al., 2010). Despite their
88 fundamental importance, the precise spatial distribution of soluble factors within
89 tissues remains unclear, due in part to a dearth of experimental techniques capable of
90 measuring diffusion *in situ*.

91
92 The emergence of super-resolution imaging in light microscopy has yielded
93 significant insights into the structure and dynamics of the immune synapse (Dustin
94 and Baldari, 2017), with the potential to elucidate the precise spatial localization of
95 soluble factors within the context of a complex tissue. These methods enable spatial
96 localization of single fluorescent probes more than an order of magnitude better than
97 the standard optical resolution limit of ~250 nm, facilitating direct visualization of
98 dynamic molecular processes. Barriers to using super-resolution for quantifying rapid
99 molecular diffusion in biological processes in the aqueous inter- and intra-cellular
100 regions in tissues include poor temporal resolution, due to constraints imposed from
101 limited photon emission, and challenges in data interpretation due to heterogeneous
102 mobility behaviors such as complex underlying diffusion modes or the presence of
103 mixed populations of molecules in multimeric forms.

104
105 To achieve the most rapid sampling possible, traditional single-molecule fluorescence
106 tracking techniques must compromise on the image quality or on the type of probe
107 used. Elastic and interferometric scattering can overcome poor fluorophore
108 photophysics to enable rapid sampling, however, they either use relatively large
109 probes that exhibit steric hindrance, or achieve poor specificity in heterogeneous
110 sample environments unless used in conjunction with fluorescent labeling (Andrecka
111 et al., 2015; Fujiwara et al., 2002; Leake, 2013; Miller et al., 2018; Piliarik and
112 Sandoghdar, 2014). Scanning fluorescence methods such as stimulated emission
113 depletion microscopy (STED (Hell and Wichmann, 1994) are limited to ~1 Hz typical
114 frame rates with faster imaging up to ~1,000 Hz possible by trading image quality
115 (Schneider et al., 2015); MINFLUX imaging (Balzarotti et al., 2017) can operate at
116 8,000 localisations per second in bacterial cells, but only tracks one molecule at a
117 time, while widefield approaches such as fast variants of photoactivatable localization
118 microscopy (PALM) (Betzig et al., 2006) and stochastic optical reconstruction
119 microscopy (STORM) (Rust et al., 2006) have integration times of on the order of
120 tens of milliseconds for individual image frames with full reconstructions commonly
121 taking several seconds. Structured illumination approaches (Gustafsson, 2000; Song
122 et al., 2016) at best have frame rates of several hundred Hz and high intensity
123 illumination methods have enabled super-resolution imaging in living cells at around
124 millisecond timescales (Plank et al., 2009; Reyes-Lamothe et al., 2010). Sub-
125 millisecond fluorescence imaging has been reported previously using relatively large
126 fluorescent bead probes (Juetten and Bewersdorf, 2010), tracking a single molecule at a
127 time (Ashley et al., 2016), in plasma membranes using fluorescently labeled
128 cholesterol analogues or Fab fragments (Hiramoto-Yamaki et al., 2014; Wieser et al.,
129 2007) and at short distances from the coverslip using TIRF and HILO imaging (van 't
130 Hoff et al., 2008). However, these methods encounter significant challenges in data
131 interpretation when samples and mobility are heterogeneous, as encountered in

132 tissues. Our method is the first, to our knowledge, to enable sub-millisecond
133 molecular tracking using a minimally perturbative nanoscale organic dye reporter in a
134 heterogeneous 3D aqueous environment typical of interstitial regions between cells in
135 tissues.

136
137 Single-molecule tracking can be used to measure diffusion coefficients of proteins
138 and molecules in localized regions and offers the opportunity to investigate the
139 heterogeneity one molecule at a time compared to the ensemble technique of
140 fluorescence recovery after photobleaching (FRAP) (Axelrod et al., 1976a, 1976b;
141 Edidin et al., 1976) and quasi single-molecule approach of fluorescence correlation
142 spectroscopy (FCS) (Ehrenberg and Rigler, 1974; Magde et al., 1972). These three
143 techniques have been compared using proteins present in the plasma membrane of
144 cells (Adkins et al., 2007; Calizo and Scarlata, 2013; Lagerholm et al., 2017; Macháň
145 et al., 2016), supported lipid bilayers (Guo et al., 2008; Macháň et al., 2016), and
146 giant unilamellar vesicles (Guo et al., 2008), which are all approximated as 2D
147 surfaces.

148
149 In this study we use single-molecule imaging approaches to quantify the diffusion of
150 the chemotactic cytokines (chemokines) CXCL13 and CCL19 (Fig. 1(b)). These
151 molecules are key regulators of lymphocyte migration that are present in spatially
152 distinct regions of the lymphoid tissues such as the lymph node (Pereira et al., 2010).
153 Chemokines are small proteins (~10kDa) that bind G-protein Coupled Receptors
154 (GPCRs) leading to polarization of the actomyosin cytoskeleton and directed
155 migration along localized concentration gradients (Rot and von Andrian, 2004).
156 Chemokine bioavailability is regulated across broad spatiotemporal scales, making
157 direct visualization of these molecules *in situ* challenging. Chemokines are secreted
158 within a dense, heterogeneous microenvironment and undergo transient interactions
159 with their cognate GPCRs and components of the extracellular matrix (ECM) before
160 undergoing receptor-mediated scavenging or enzymatic degradation (Colditz et al.,
161 2007; Rot and von Andrian, 2004; Schulz et al., 2016). In addition, chemokines are
162 heterogeneous in their binding affinities and are subject to multimerization effects;
163 characteristics that may alter their mobility (Bennett et al., 2011; von Hundelshausen
164 et al., 2017). Simplified hydrodynamic predications (Einstein, 1905) employing
165 estimations for the Stokes radius of chemokines and the fluid environment viscosity
166 suggest that chemokine diffusion in hypothetically homogeneous intracellular media
167 in the absence of binding effects would be rapid at $\sim 150 \mu\text{m}^2/\text{s}$, implying ~ 50 s for a
168 single molecule to diffuse across a $200 \mu\text{m}$ diameter region of lymphoid tissue.
169 However, this estimate is likely to be a poor predictor of diffusivity, as it does not
170 account for dynamic molecular interactions encountered in dense, heterogeneous
171 tissues.

172 In the following sections we describe a method to overcome previous technological
173 barriers to the study of molecular mobility *in situ*. Specifically, we have adapted a
174 standard inverted epifluorescence microscope, making important modifications to
175 facilitate minimally perturbative sub-millisecond single-molecule tracking of rapidly
176 diffusing fluorescently labeled biomolecules via sub-diffraction limit localizations,
177 and developed bespoke software for precise quantification of underlying molecular
178 mobility of tracked particles. We compared FCS, FRAP and single molecule tracking
179 on the well-characterized test system for molecular mobility of bovine serum albumin
180 (BSA), labeled with Alexa Fluor 647 (AF647). We then applied our method to

181 quantify the diffusion of CCL19 and CXCL13 (Fig. 1b), in a range of environments of
182 increasing complexity comprising (i) buffer alone and in the presence of the highly-
183 branched polysaccharide Ficoll to vary the fluid environment viscosity, (ii) the
184 presence of either surface-immobilized heparan sulfate, or a collagen gel matrix, and
185 further (iii) AF647 tagged CXCL13 was tracked in an *ex vivo* native mouse lymph
186 node environment. Our data suggests that CCL19 and CXCL13 have distinct diffusion
187 rates, and that CXCL13 exhibits both specific binding and diffusion at $6.6 \pm 0.4 \mu\text{m}^2\text{s}^{-1}$
188 within the B-cell follicle.

191 **Results**

193 **Overview of the high-speed single-molecule tracking methodology**

194
195 To enable precise localization and tracking of rapidly diffusing biomolecules we
196 modified the optical path of a standard inverted epifluorescence microscope (Fig.
197 1(a)) to implement a broadband laser whose output was selectable over wavelengths
198 ~400-2,000 nm (Supplementary Fig. 1), spanning the excitation spectra of visible
199 light and near infrared fluorophores; the beam was de-expanded using a series of
200 lenses to generate a narrow illumination field of ~12 μm full width at half maximum
201 which could be switched from epifluorescence into total internal reflection
202 fluorescence (TIRF) by controllable translation of a lens, although TIRF was not used
203 in this work. High contrast epifluorescence images magnified to 120 nm/pixel were
204 captured by an ultrasensitive back-illuminated EMCCD detector (860 iXon+, Andor
205 Technology Ltd.) which could be sub-arrayed to 29x128 pixels to enable rapid frame
206 rates of 1,515 Hz. Images were analyzed using bespoke software (Miller et al., 2015)
207 written in MATLAB (Mathworks), which enabled automated 2D sub-millisecond
208 tracking of single fluorescent dye molecules and determination of the microscopic
209 diffusion coefficient D from the measured mean square displacement (Robson et al.,
210 2013). Diffusion coefficients were found by an iterative fitting procedure developed
211 with simulated data.

214 **Speed of tracking and image analysis**

215
216 A range of sample exposure times of 0.44-1.98 ms per frame were used, with most
217 data acquired at 0.59 ms per frame (0.65 ms cycle time) as a compromise between
218 sampling speed and localization precision. In all cases we were able to resolve distinct
219 diffusing fluorescent foci of measured 2D half width at half maximum in the range
220 250-300 nm, consistent with single point spread function (PSF) images. Automated
221 foci tracking was utilized for the determination of molecular diffusivity. Foci could be
222 tracked continuously in 2D with ~40 nm precision (Supplementary Fig. 4).

223
224 The presence of single molecules was determined by the observation of stepwise
225 photobleaching steps. Examples of this are shown in Supplementary Fig. S1c,d,. From
226 the manufacturers specifications BSA-AF647 was expected to be labeled with
227 between 3-6 AF647 dye molecules and the chemokines were expected to be singly
228 labeled. Only single molecule bleaching steps were observed in the chemokine data.

229

230 The initial intensity of observed foci of the AF647 dye molecule was measured in five
231 conditions: CCL19-AF647 and CXCL13-AF647 in collagen and under heparan
232 sulfate immobilization, and BSA-AF647 in 10% Ficoll. The kernel density estimate
233 was found from the intercept of a line fitted to the first three intensity values
234 measured. Within experimental error the initial intensity for all conditions fell in the
235 2000-3000 count range. The initial intensity is expected to vary for each condition due
236 to the different local environment of the AF647 tag on each molecule, including
237 different allowed orientations and varying flexibility of the linker. Further, the
238 viscosity of the medium is known to affect the emission profile of AF647 and will
239 cause slight variations in total measured intensity due to the use of a band pass filter
240 in the emission path.

241
242 Analysis of the tracking data from CXCL13-AF647 and CCL19-AF647 using step-
243 wise dye photobleaching showed predominantly monomeric populations for each
244 (Fig. 2, Supplementary Fig. 1). Apparent stoichiometry values determined from the
245 intensity of tracked fluorescent foci greater than one molecule per foci may be due to
246 real multimeric complexes or potentially due to the overlap of monomeric foci images
247 in the 2D projection that is imaged, especially in the case of high dye concentration.
248 The maximum number of detected foci in one frame of 15 foci in our case was used in
249 a random overlap model which assumes a Poisson distribution for nearest neighbor
250 foci overlap probability (Llorente-Garcia et al., 2014; Wollman et al., 2017). This
251 analysis indicates an 18% probability for random single foci overlap. The predicted
252 intensity of foci due to random overlap could be obtained by convolving the intensity
253 distribution of a single molecule of AF647 (width scaled by the square root of the
254 apparent stoichiometry) with the apparent stoichiometry distribution generated by the
255 random overlap probability prediction. The overlap model was found to be
256 statistically identical to the experimentally observed distribution below apparent
257 stoichiometry values of six AF647 molecules per foci ($p < 0.05$, Pearson's χ^2 test). A
258 small proportion of less than 5% of foci we found to have a higher apparent
259 stoichiometry than that predicted from the random overlap model; it is possible that
260 these may be indicative of some additional factors not captured in the basic overlap
261 model such as non-uniformity in illumination across the field of view and
262 experimental autofluorescence.

263

264 **Iterative data simulation and experimental data fitting**

265

266 Our analysis of the distribution of effective diffusion coefficients obtained from the
267 single-molecule tracking data was corroborated through simulations of diffusing and
268 immobilized foci using realistic signal and background noise values. Iterative cycles
269 of simulation and experimental data fitting were used to determine initial parameters
270 for fitting and the form of the fitting functions. All simulations were run and fitted
271 with and without the addition of Gaussian white noise. The first simulated values
272 were chosen by fitting the experimental data with a two gamma distribution model
273 (Qian et al., 1991) to account for two diffusive populations.

274

275 Initially two distributions; $1.6 \mu\text{m}^2\text{s}^{-1}$ and a 50:50 mixed population of $1.6 \mu\text{m}^2\text{s}^{-1}$ and
276 $10 \mu\text{m}^2\text{s}^{-1}$ were simulated (sample images in Fig. 3a). The data was plotted via kernel
277 density estimation, and fitted with 1, 2 and 3 gamma distribution functions with 4
278 independent steps, all parameters constrained to be positive, each term was multiplied
279 by a fractional prefactor to preserve the unity area of the kernel density plot, and the

280 χ^2 goodness-of-fit parameter was evaluated (Supplementary Table 1). The χ^2 statistic
281 accounts for the number of free parameters in the fit, and is used to determine if
282 decreasing residuals are caused by increasing the number of free parameters. For the
283 one component distribution the one gamma fit gave the lowest χ^2 , and for the two
284 component distribution, the two gamma fit gave the lowest χ^2 value, as expected.
285 Applying these three models to the experimental collagen and heparan sulfate
286 immobilized chemokine data gave the lowest χ^2 for a two component fit, except for
287 CCL19 in heparan sulfate, which contained a very low proportion of mobile tracks
288 and was well fitted by a single component distribution. From this, it was determined
289 that a two component distribution should be fitted to the experimental data.

290
291 The number of independent steps is usually taken to be the same as the number of
292 steps analyzed in gamma distribution fitting analysis of microscopic diffusion
293 coefficients, where it is a parameter governing the shape of the distribution. Strictly,
294 steps are only independent when non-overlapping steps are used (Qian et al., 1991),
295 but when the localization precision (in nm) of single particles is small compared to the
296 distance moved between localizations in a track the diffusion coefficient distributions
297 from overlapping steps are still well-approximated by the assumption of independent
298 steps. In this work, the temporal resolution is increased to a level where the
299 localization precision is no longer negligible compared to the distance moved between
300 localizations, and steps containing the same localizations are no longer well
301 approximated as being independent. To investigate the independence of the steps in
302 the data and determine the relevant fitting parameter, simulations of $1.6 \mu\text{m}^2\text{s}^{-1}$ and 10
303 $\mu\text{m}^2\text{s}^{-1}$ were made separately, and fitted with a single component gamma distribution
304 where the number of independent steps was allowed to vary. The results (Table 1)
305 indicate this value to be around two, in line with expectations of consecutive steps
306 containing the same localization not being independent, reducing the number of steps
307 by half.

308
309 Fitting simulations of a 50:50 population of molecules with diffusion coefficients of
310 $1.6 \mu\text{m}^2\text{s}^{-1}$ and $10 \mu\text{m}^2\text{s}^{-1}$ with two gamma distributions with the same fitted value of N
311 in each distribution, and N constrained to be in the range 0-4, (Fig. 3b and
312 Supplementary Table 2), gives a distribution which does not match the experimental
313 data (Fig. 4a, 5d-e): when the data is placed in a histogram based on measured
314 diffusion coefficient the experimental data shows a peak in the first bin width, which
315 is not seen in the simulation of $1.6 \mu\text{m}^2\text{s}^{-1}$ data. The $1.6 \mu\text{m}^2\text{s}^{-1}$ data was simulated
316 because this was found as a preliminary result of fitting to the experimental data, but a
317 simulation of truly immobile data with a diffusion coefficient of $0 \mu\text{m}^2\text{s}^{-1}$ gave a peak
318 in the first bin of the histogram when put into bins with the width of the localization
319 precision (see Fig. 3c), matching the experimental data.

320
321 Our simulated particle diffusion analysis suggests that the low mobility population in
322 the experimental data is immobile at the level of the localization precision. Fitting the
323 distribution of simulated $0 \mu\text{m}^2\text{s}^{-1}$ data with a single gamma distribution gave a value
324 of N less than one, and requires the fit applied to the experimental data to include a
325 different value of N in the distribution fitted to each population; with the value of N
326 being less than one for the low mobility population, and two for the higher mobility
327 population.

328

329 Applying this fit, with the constraint that the diffusion coefficient of the immobile
330 population must fall within the first bin of the histogram, gave the fitted experimental
331 diffusion coefficients. To qualitatively compare the simulated and experimental data,
332 a mixed simulation of 0 and $9 \mu\text{m}^2\text{s}^{-1}$ data with Gaussian white noise was performed
333 and fitted in the same way, giving a diffusion coefficient for the mobile peak of
334 $8.9 \pm 0.4 \mu\text{m}^2\text{s}^{-1}$. The distribution is similar in profile to the data for CCL19-AF647 in
335 collagen (see Fig. 3d).

336

337 **Diffusion in buffer and Ficoll solutions**

338

339 In PBS buffer alone the chemokine diffusion was in general too fast to track over
340 consecutive image frames (Supplementary Video 1). Whilst this is consistent with
341 theoretical estimates using the Stokes-Einstein relation which gives $D \sim 150 \mu\text{m}^2/\text{s}$ for
342 chemokines in an aqueous environment, the application of 10% Ficoll increased the
343 fluid viscosity by a factor of 5.6 to 0.005 Pa.s, which enabled single particle tracking;
344 if diffusion had been well modelled by the Stokes-Einstein relation the diffusion
345 coefficients in the higher viscosity Ficoll solution would be expected to be $\sim 30 \mu\text{m}^2/\text{s}$
346 and particles would still not be tracked. The ability to track single chemokines in a
347 medium of this viscosity demonstrates that the theory is not adequate to describe
348 chemokine diffusion and motivates our experimental measurements.

349

350 The experimental system was tested first on a non-chemokine control of AF647-
351 tagged BSA (BSA-AF647). The results of single particle tracking of BSA-AF647
352 were consistent with a proportion of immobile tracks associated with the coverslip
353 surface and a freely diffusing mobile population with $D_{\text{mobile}} = 9.3 \pm 0.4 \mu\text{m}^2\text{s}^{-1}$ (Fig. 4
354 and Supplementary Video 2,3). Including theoretical expectations based on
355 hydrodynamic modeling of BSA as a Stokes sphere of radius 3.48 nm for monomeric
356 BSA, with a monomer to dimer ratio of 15:2 (measured using SEC-MALLS
357 quantification, Supplementary Fig. 2 Supplementary Table 3) and incorporating
358 Faxen's law for distances of 10 nm, at which distances increased viscosity effects
359 occur at the coverslip boundary (Axelsson, 1978), the fitted mobile value is found to
360 be in agreement with the theoretical value of $9.4 \mu\text{m}^2\text{s}^{-1}$.

361

362 **Comparison of SMT with FCS and FRAP**

363

364 The diffusion coefficient of AF647 labeled BSA in a Ficoll solution was additionally
365 measured with FCS and FRAP to generate a comparison of the three methods in a
366 complex, non-surface environment (Supplementary Fig. 3a-e). FRAP and FCS gave
367 diffusion coefficients of $7.1 \pm 0.3 \mu\text{m}^2\text{s}^{-1}$ and $18.8 \pm 0.3 \mu\text{m}^2\text{s}^{-1}$ respectively
368 (Fig. 4b,c, Table 2). The values found for the diffusion coefficients by these methods
369 are summarized in Table 1 with the number of traces used for each measurement. The
370 result for FCS is higher than the theoretical value, whilst that for FRAP is
371 significantly lower even considering Faxen's law, temperature fluctuation and non-
372 monomer content in BSA measured by SEC-MALLS (Supplementary Fig. 2 and
373 Supplementary Table 3), however the effects of using an axially thin sample and
374 including only 2D recovery in the FRAP analysis were not accounted for.

375

376 The FRAP and FCS results differ by a factor of 2.6, in general agreement with
377 previous results from others in which diffusion coefficients found by FCS are mostly
378 higher than those found by FRAP (Guo et al., 2008), with FCS giving values up to an

379 order of magnitude higher than the values found by FRAP (Adkins et al., 2007; Calizo
380 and Scarlata, 2013) and often attributed to the different spatial scales of the two
381 measurements or the high number of assumptions required in fitting FRAP data
382 (Macháň et al., 2016), such as the profile of the bleaching laser, which are likely to be
383 factors in the experiments performed here. The value found by SMT was the closest
384 to the theoretical estimate of the diffusion coefficient in Ficoll of the experimental
385 viscosity.

386

387 FCS and FRAP were also performed on the chemokines in 10% Ficoll 400. FCS
388 produced autocorrelation curves with similar amplitude to BSA-AF647, but high
389 variation was observed in the relative sizes and characteristic decay times of the
390 triplet and translational diffusion populations (Supplementary figure 3f), resulting in
391 no consensus value of the diffusion coefficient. Both FCS and FRAP measurements
392 were hindered by the presence of large multimers of chemokine (Supplementary Fig.
393 3g). Multimers of this type are simply avoided by visual identification in single
394 molecule tracking experiments.

395

396 **Diffusion coefficients of CXCL13 and CCL19 in collagen**

397

398 The values of the diffusion coefficients were determined in collagen reconstituted
399 from rat tails to produce a simplified tissue mimic. The structure of the collagen was
400 checked for the required formation of non-centrosymmetric structure with second-
401 harmonic imaging microscopy (SHIM) (see Fig. 5a,b). The fibril diameters observed
402 are in agreement with those seen by Chen *et al.* (Chen et al., 2012), and show
403 qualitatively similar structure.

404

405 The values of the diffusion coefficients of CXCL13 and CCL19 in collagen were
406 found by fitting a two gamma distribution to a histogram of the single-molecule
407 tracking data with bin width of 40 nm given by peaks in the localization precision at
408 low diffusion coefficient found from heparan sulfate immobilization of the labelled
409 chemokines (Supplementary Fig. 4a,b, Supplementary videos 7,8). Heparan sulfate
410 immobilization was verified by an extremely high proportion of immobile tracks
411 (Supplementary Fig. 4c,d). The results of the fitting are given in Table 3, and the
412 distributions for each chemokine showing the mobile and immobile populations are
413 shown in Fig. 5c-e with sample images shown in Fig. 5c. The relative size of the
414 mobile and immobile populations cannot be accurately accounted for as immobile
415 populations were photobleached to enable imaging of highly diffuse mobile
416 populations.

417

418 Modeling the sub-millisecond tracking data as a mixture of immobilized and mobile
419 tracks generated excellent agreement to the experimental data (Table 3). Our findings
420 indicated a higher diffusion coefficient for CCL19-AF647 than for CXCL13-AF647
421 in the controlled environment of collagen (Fig. 5f and Supplementary Videos 4,5),
422 which we measured as $8.4 \pm 0.2 \mu\text{m}^2\text{s}^{-1}$ and $6.2 \pm 0.3 \mu\text{m}^2\text{s}^{-1}$ respectively. This
423 heterogeneity is consistent with molecular mass expectations and may contribute to
424 the formation of distinct spatial patterning profiles *in situ*.

425

426 **Binding of CXCL13 to lymph node tissue sections**

427

428 The experiments with BSA-AF647, CCL19-AF647 and CXCL13-AF647 in collagen
429 suggested a 4-6 times higher proportion of molecules in the immobile fraction than
430 the mobile fraction for the chemokines than for BSA-AF647, even allowing for
431 differences introduced by utilizing a pre-bleach to increase the fraction of mobile
432 tracks. This is in agreement with previous results: CXCL13 is secreted in soluble
433 form, but is known to interact with extracellular matrix components (Monneau et al.,
434 2017) and thus is likely to comprise a significant immobile fraction. To assess both
435 fractions while also ensuring a sufficiently low concentration of CXCL13-AF647 to
436 enable single molecule detection, we incubated murine lymph node tissue
437 cryosections with CXCL13-AF647 and performed a short wash step. Whilst removing
438 a large component of the soluble fraction of CXCL13-AF647, this preparation
439 facilitated tracking of both mobile and immobile fractions of CXCL13-AF647 *in situ*,
440 depending on the microscopy method employed.

441

442 To assess the specificity of binding we used confocal microscopy to quantify the
443 fluorescent intensity of B220⁺ regions (Fig. 6a) of lymph node tissue sections that had
444 been incubated with either CXCL13-AF647 or BSA-AF647. The fluorescent intensity
445 values obtained were significantly higher for samples incubated with CXCL13-AF647
446 (Fig. 6b,c), suggesting that the binding of CXCL13 to lymph node follicles was
447 specific.

448

449 In the single molecule microscopy experiments we imaged and tracked CXCL13-
450 AF647 in B cell follicles of *ex vivo* murine lymph node tissue sections with super-
451 resolution precision at ~2 ms timescales (Fig. 7c and Supplementary Video 6),
452 determining the precise location in the tissue using FITCB220 (B cell specific marker)
453 (Supplementary Fig. 5). Auto-fluorescent extracellular matrix (ECM) components
454 were localized by the tracking software and were segmented to allow discrimination
455 of tracks from the immobile ECM and the diffusing chemokine (Fig. 7c,d,f). When
456 the same segmentation analysis was performed on control tissue sections prepared by
457 the same protocol except without the addition of CXCL13-AF647, similar
458 autofluorescent structures were seen and could be segmented (see Fig. 7a,b). The
459 observed diffusion coefficient distribution of tracked extracellular matrix regions
460 within the B-cell follicle in the presence of chemokine were observed to be skewed
461 towards higher mobility than those in the absence of chemokine (Fig. 7e), further
462 confirming the presence of specific binding of CXCL13-AF647 in the extracellular
463 matrix regions.

464

465 **Diffusion coefficient of CXCL13 in lymph node tissue sections**

466

467 For the same single-molecule imaging experiments performed at at ~2 ms timescales
468 described above, after discrimination of mobile and immobile tracks by segmentation,
469 the diffusion coefficient of mobile tracked particles for the field of view shown was
470 fitted with a single gamma distribution indicating $D = 6.6 \pm 0.4 \mu\text{m}^2\text{s}^{-1}$ (Fig. 7g). Due
471 to the inclusion of a wash step in our sample preparation we expect the majority of the
472 mobile particles to be in the interstitial spaces between cells, although a small fraction
473 may be within cut cells due to the preparation of tissue sections. The lack of
474 fluorescent localizations in the central gap in the control sample is further evidence
475 that the mobile population observed in the data is CXCL13-AF647.

476

477 To validate our result we performed a simulation of the conditions in the tissue, with
478 the mean background level and standard deviation of the noise taken from the control
479 data. 1000 frames of data of particles with diffusion coefficient $6.6 \mu\text{m}^2\text{s}^{-1}$ were
480 generated, with spot intensities and spot widths taken from the experimental data for
481 tracking in tissue. Sample images from the simulation can be seen in supplementary
482 figure 6(a). The result of fitting this simulation was $D = 7.0 \pm 0.4 \mu\text{m}^2\text{s}^{-1}$
483 (supplementary figure 6(b)), in agreement with the simulated value. Taken together,
484 this demonstrates the ability of our method to extract diffusion coefficients from
485 challenging experimental data.
486

In review

487 Discussion

488

489 In this work, we have demonstrated the application of a high-speed single-molecule
490 tracking microscopy system that is compatible with traditional widefield light
491 microscopes. We compared our method with the traditional methods to measure
492 molecular mobility of FCS and FRAP using one of the standard test molecules for
493 molecular mobility (BSA). We applied this new approach to investigating hitherto
494 unquantified molecular mobility of chemokines in complex environments, finding
495 values of diffusion coefficients of $8.4 \pm 0.2 \mu\text{m}^2\text{s}^{-1}$ for CCL19-AF647 and 6.2 ± 0.3
496 $\mu\text{m}^2\text{s}^{-1}$ for CXCL13-AF647 in collagen, and of $6.6 \pm 0.4 \mu\text{m}^2\text{s}^{-1}$ for CXCL13-AF647
497 in lymph node follicles, in addition to identifying a specifically bound CXCL13-
498 AF647 population in the B-cell follicle. While we demonstrate the efficacy of the
499 approach on chemokines, this is a proof-of-concept for a more general scheme that
500 could be applied to signaling lipids and cytokines.

501

502 Our method enables single-molecule tracking of organic dye probes at sub-
503 millisecond timescales, down to less than half a millisecond per imaging frame whilst
504 still enabling 40 nm localization precision in realistic tissue mimetic
505 microenvironments. In *ex vivo* lymph node tissue sections, we were able to perform
506 rapid super-resolution sampling down to 2ms per imaging frame and still achieve
507 single-molecule detection sensitivity. To our knowledge this is the first application of
508 sub-millisecond tracking of small fluorophores away from the coverslip interface.

509

510 We characterized the output of our single-molecule tracking tools with a range of
511 simulations of mixed molecular mobility using realistic levels of signal and noise
512 comparable to those exhibited at challenging single-molecule detection levels with
513 very rapid sub-millisecond fluorescence sampling. We also tested our imaging and
514 analysis methods using a fluorescently labeled version of the well-characterized
515 molecule, BSA, and compared these with experiments using FRAP and FCS. The
516 values of diffusion coefficient for mobile BSA determined using our rapid SMT
517 method were in close agreement to expectations based on hydrodynamic modeling.
518 Equivalent BSA mobility values estimated from using FRAP or FCS were less
519 reliable. We compared the diffusion coefficients of BSA-AF647 measured by FCS,
520 FRAP and SMT, producing a comparison of these techniques away from the coverslip
521 interface, and showing agreement in the relation of the measured values with most
522 previous studies performed on lipid bilayers, or on live cell plasma membranes.

523

524 We measured the diffusion coefficients of CXCL13-AF647 and CCL19-AF647 in
525 reconstituted collagen, finding values of $6.2 \pm 0.3 \mu\text{m}^2\text{s}^{-1}$ and $8.4 \pm 0.2 \mu\text{m}^2\text{s}^{-1}$
526 respectively. We further measured the diffusion coefficient of CXCL13-AF647 in *ex*
527 *vivo* lymph node tissue section, finding a value in agreement with that measured in
528 collagen of $6.6 \pm 0.4 \mu\text{m}^2\text{s}^{-1}$. Fluorescent tags increase the mass of the labelled
529 molecule and potentially affect the properties of diffusion. The fluorophore used in
530 this work, AF647, was chosen for its small mass, which is especially important here
531 given the small mass of chemokines. This choice resulted in a ~10% increase in mass
532 of the labelled chemokine compared to the unlabeled chemokine, but this is lower
533 than would have been achieved with other fluorophores. Following the assumptions of
534 the Stokes-Einstein model of a spherical protein of uniform density, a 10% increase in
535 mass would only decrease the observed diffusion coefficient by ~3.2%. We observe a
536 large discrepancy between our empirical measurements for chemokine diffusion rates

537 and the higher estimated values derived on the basis of Stokes-Einstein relation.
538 However, this discrepancy is of the same order of magnitude as that previously
539 observed for the same theoretical calculation for GFP ($\sim 93 \mu\text{m}^2\text{s}^{-1}$) and measured
540 experimental values in Escherichia Coli ($\sim 7.7\text{-}9 \mu\text{m}^2\text{s}^{-1}$ (Elowitz et al., 1999;
541 Mullineaux et al., 2006)). This discrepancy may be indicative of additional factors that
542 affect molecular mobility in tissues but are not captured in the simplistic Stokes-
543 Einstein relation. These factors might include, for example, dynamic physical and
544 chemical processes which result in more constrained mobility such as transient
545 biochemical interactions within the localized microenvironment, as have been
546 observed previously in studies which suggest that CXCL13 binds to extracellular
547 matrix components (Monneau et al., 2017).

548

549 Placed in an immunological context, our data shows that chemokine mobility is
550 multimodal in complex environments. Using our novel imaging approach we were
551 able to quantitatively identify a mobile and immobile fraction in collagen, and using a
552 combination of confocal microscopy and single-molecule imaging we identified
553 mobile and bound populations of CXCL13-AF647 in lymph node follicles. Thus, it is
554 important to consider the contributions of both populations of CXCL13 upon cellular
555 behaviors, rather than taking a view where it acts in either a soluble or an immobile
556 way. The properties, and likely highly constrained nature of CXCL13 diffusion within
557 the follicle may provide an insight into how B-cells can form such tightly
558 compartmentalized microanatomical structures such as the follicle, or the germinal
559 center light-zone.

560 Our novel high-speed microscopy and analysis outperforms traditional molecular
561 mobility tools of fluorescence recovery after photobleaching (FRAP) and
562 fluorescence correlation spectroscopy (FCS) in being able to capture diffusional
563 heterogeneity relevant to real, complex biological systems exemplified by underlying
564 mobile and immobile states. The high time resolution achieved with our system
565 enables rapid diffusion to be quantified in heterogeneous aqueous environments
566 typical of interstitial regions between cells in tissues, whilst still retaining super-
567 resolution spatial precision and single-molecule detection sensitivity, enabling new
568 insight into complex systems. A key advantage of our rapid single particle tracking
569 method is its ability to determine the underlying heterogeneity in the mobility of the
570 molecular population exemplified here by chemokines that diffuse in different
571 environments. Whilst we demonstrate the efficacy of the approach on chemokines,
572 this is a proof-of-concept for a more general scheme that could be applied to lipids
573 and cytokines. Our system is compatible with traditional widefield light microscopes
574 as opposed to requiring expensive and dedicated super-resolution setups; this
575 accessibility bodes well for establishing a significant future impact investigating
576 multiple biological systems.

577

578 **Materials and Methods**

579 **Reagents**

580 Human CXCL13 and CCL19 (Almac, CAF-12 and CAF-06 respectively) singly
581 labeled with the far-red fluorescent tag AF647 (molecular mass 1250 Da) were stored

582 in water at 222 μ g/ml. This fluorophore was chosen because of its small molecular
583 mass, which reduces the impact of increased mass on molecular mobility, and due to
584 its excitation at the long, lower energy wavelength range of the spectrum, which
585 reduces sample damage. Collagen samples contained type I collagen extracted from
586 rat tails (Barnes et al., 2016) diluted in PBS to 3.3 mg/ml and chemokine at 111
587 ng/ml; samples were set to pH7 with the addition of NaOH. BSA labeled with 3-6
588 AF647 purchased from Thermo Fisher Scientific Inc. Ficoll 400 (Sigma-Aldrich) was
589 diluted in PBS at 0.1g/ml to create a 10% solution of viscosity 0.005 Pa.s at room
590 temperature (Rashid et al., 2015).

591

592 **Preparation of collagen matrix in tunnel slides**

593 Samples for fluorescence microscopy were prepared in tunnel slides formed by
594 placing two parallel lines of double-sided tape on a standard microscopy slide around
595 5 mm apart. A plasma-cleaned coverslip was placed on top and carefully tapped down
596 (avoiding the imaging area) to create a water-tight tunnel.

597 For imaging in a collagen matrix tunnel slides were cooled to 4°C before addition of
598 collagen and fluorescently labeled chemokines, and then incubated at 15°C for
599 30 min, followed by an additional 30 min incubation at 37°C. The collagen matrix
600 was visualized using second harmonic imaging (Chen et al., 2012; Cox et al., 2003).

601 Immobilized chemokine samples were prepared by incubating a plasma-cleaned
602 coverslip in heparan sulfate (Simon Davis and Parish, 2013) (50 mg/ml) (Sigma-
603 Aldrich) in PBS for 30 min. Coverslips were washed with PBS and air dried for 30
604 min before tunnel slide assembly then 10nM fluorescently labeled chemokine solution
605 in PBS was introduced to the tunnel slide and incubated in a humidity chamber for 15
606 min at 20°C. Excess unbound chemokine was removed with a PBS wash.

607

608 **SHIM imaging**

609

610 Second harmonic imaging microscopy (SHIM) was performed on a Zeiss LSM 780
611 MP with a Zeiss invert microscope. Excitation at 900 nm wavelength (Coherent Ultra
612 Laser) through a plan-apochromat 63x/1.4 oil objective lens was incident on the
613 sample. Up converted light was collected via a 485 nm short pass filter onto a non-
614 descanned detector.

615

616 **Preparation of Lymph Node Tissue Sections**

617

618 6-8 week old wild type mice (C57BL/6) were housed in BSF at the University of
619 York. All experiments conformed to the ethical principles and guidelines approved by
620 the University of York Institutional and Animal Care Use Committee. Popliteal
621 Lymph Nodes were removed and excess fat or connective tissue removed with
622 forceps. Samples were transferred to optimal cutting temperature medium (OCT,
623 Tissue-Tek, Sakura Finetek) and snap frozen on dry ice samples and sectioned using a
624 cryostat. 10 μ m thick sections were cut and collected onto poly-L-Lysine coated
625 microscope slides. Sections were dried overnight in the dark then stored at -20°C.

626 Before use, lymph node sections on poly-L-lysine slides were incubated at room
627 temperature for 30 min. Sections were hydrated in PBS for 5 min then air dried. Wax
628 ImmEdge pen (Vector Laboratories) was used to draw a hydrophobic circle around

629 each section to retain liquid on the section during staining. Sections were incubated in
630 a blocking buffer of PBS 5% goat serum (Sigma) at room temperature for 1 hour. To
631 determine where B cell follicular structures were located in the tissue we used the
632 marker B220, a protein expressed on the surface of all murine B lymphocytes. After
633 blocking, sections were incubated with an FITC conjugated antibody (RA3-6B2,
634 purchased from eBioscience) that binds specifically to B220 diluted 1:200 in blocking
635 buffer for 1 hour at room temperature. . After blocking, sections were incubated with
636 an FITC conjugated antibody (RA3-6B2, purchased from eBioscience) that binds
637 specifically to B220 diluted 1:200 in blocking buffer for 1 hour at room
638 temperature. Samples were washed with PBS for 3 x 5 min.

639
640 For confocal microscopy experiments where exogeneous CXCL13-AF647/BSA-
641 AF647 was used to measure binding to tissue, slides were stained with anti-B220 as
642 described above followed by an incubation with 500nM of each fluorescently labelled
643 protein for 1 hour at room temperature. Samples were then washed 1x 5 mins in PBS.
644 A drop of Prolong gold (Invitrogen) was added to each section, and then a No 1.5
645 glass coverslip (Fisher) mounted on top. The slides were incubated overnight at 4°C
646 the next day slides were sealed using nail varnish and stored at 4°C.
647 Immunofluorescent stained sections were imaged using the Zeiss LSM 880 confocal
648 microscope.

649
650 For single-molecule microscopy experiments sections were stained for B220 as
651 described above, and then 1 μ M of CXCL13-AF647 was added to the slides. Slides
652 were incubated overnight at 4°C after which slides were washed for 30 s in PBS and a
653 coverslip (thickness 0.13-0.17mm, Menzel Gläser) mounted on top. Slides were then
654 sealed and imaged.

655 **Stokes model of diffusion**

656 For a small sphere the diffusion coefficient is given by:

658

$$D = \frac{k_B T}{6\pi\eta r}$$

659

660 where k_B is the Boltzmann constant, T is room temperature, η is the dynamic
661 viscosity of the media and r is the radius of a sphere, calculated assuming that the
662 molecule is a globular protein of density 1.35 g.cm⁻³ (Fischer et al., 2004). The
663 theoretical value of the diffusion coefficient of BSA in 10% Ficoll 400 was
664 calculated using the Stokes radius of BSA of 3.48nm (Ikeda and Nishinari, 2000). The
665 Stokes radius of a dimer was assumed be double the Stokes radius of a monomer.

666

667 **Faxen's Law**

668 At distances probed by narrowfield fluorescence microscopy (~ few hundred
669 nanometres of the coverslip), the boundary effect of increased viscosity in the
670 solution can be modeled by Faxen's law (Happel and Brenner, 1981):

671

$$\eta(h) = \eta(\infty) \left(1 + P \left(\frac{r}{h} \right) \right)^{-1}$$

672 where $\eta^{(\infty)}$ = dynamic laminar-flow viscosity in free solution, r is the radius of the
 673 particle, and h is the distance between the boundary and the center of the particle. To
 674 a 5th-order approximation:

$$675 \quad P(\gamma) \approx -\frac{9\gamma}{16} + \left(\frac{\gamma}{8}\right)^3 - \left(\frac{45\gamma}{256}\right)^4 + \left(\frac{\gamma}{16}\right)^5$$

676

677 **SEC-MALLS of BSA-AF647**

678

679 The experimental system for SEC-MALLS experiments comprised a Wyatt
 680 HELEOS-II multi-angle light scattering detector and a Wyatt rEX refractive index
 681 detector attached to a Shimadzu HPLC system (SPD-20A UV detector, LC20-AD
 682 isocratic pump system, DGU-20A3 degasser and SIL-20A autosampler). 100 μ l of
 683 2.5 mg/ml BSA-AF647 sample was run at 0.5 ml/min flow rate at room temperature
 684 through superdex S200 columns (G.E. Healthcare) for 60 min in PBS running buffer.
 685 Peaks were integrated using Astra V software and the Zimm fit method with degree 1;
 686 a value of 0.183 was used for protein refractive index increment (dn/dc).

687

688 **FCS and FRAP microscopy**

689 FCS and FRAP experiments were performed on a Zeiss LSM 880 microscope, using a
 690 GaAsP detector. Samples were prepared in MatTek glass bottom petri dishes (1.5
 691 coverglass, MatTek Corporation) and illuminated with a 633 nm wavelength laser.

692

693 For FCS the confocal volume was measured using a calibration sample of BSA-
 694 AF647 diffusion in water and constraining the diffusion coefficient to be $59 \mu\text{m}^2\text{s}^{-1}$
 695 (Putnam, 1975); this allowed the structural parameter, s , to be fixed at 6.6. Three
 696 repeats of ten experiments were conducted, traces indicating the presence of
 697 multimeric clumps or proximity to the surface were excluded. Autocorrelation traces,
 698 $G(\tau)$, to account for transient dark states and translational diffusion were fitted with
 699 the equation:

$$G(\tau) = 1 + \left(1 + \frac{T e^{-\left(\frac{\tau}{\tau_T}\right)}}{1 - T}\right) \left(\frac{1}{V_{eff} \langle C \rangle} \frac{1}{\left(1 + \frac{\tau}{\tau_D}\right)} \frac{1}{\sqrt{1 + \left(\frac{1}{s}\right)^2 \frac{\tau}{\tau_D}}} \right)$$

700 where T is the triplet fraction, τ_T is the time constant of the dark state, τ_D is the time
 701 constant of translation across the confocal volume, V_{eff} , and $\langle C \rangle$ is the average
 702 concentration. The diffusion coefficient, D , was calculated from τ_D via the equation:
 703

$$D_{FCS} = \frac{r_0^2}{4\tau_D}$$

704

705 where r_0 is the spot width (0.322 μm). For FRAP microscopy a square region defined
 706 in the Zeiss Zen software was bleached with the 633 nm wavelength focused laser in

707 an axially thin sample that was treated as being 2D. When applied to immobilized
708 fluorophore the shape of the bleached area (see Fig. 4b) was found to be well
709 approximated as a Gaussian spot of half-width $\omega = 4.9 \pm 0.1 \mu\text{m}$. To measure the
710 diffusion coefficient of BSA-AF647 thirty recovery traces (intensity (I) vs time (t))
711 were acquired and fitted in the Zeiss Zen software with the single exponential
712 equation:

$$I = I_0 - I_1 e^{\left(-\frac{t}{\tau_1}\right)}$$

714 where the initial intensity, I_0 , drop in intensity, I_1 , and the decay constant τ_1 , from
715 which the diffusion coefficient, D , is calculated via:

$$D_{FRAP} = \frac{\omega^2}{8\tau_1}$$

718

719 **Single molecule fluorescence microscopy**

720

721 Bespoke fluorescence microscopy was performed on an inverted microscope body
722 (Nikon Eclipse Ti-S) with a 100x NA 1.49 Nikon oil immersion lens and illumination
723 from a supercontinuum laser (Fianium SC-400-6, Fianium Ltd.), controlled with an
724 acousto-optical tunable filter (AOTF) to produce excitation light centered on
725 wavelength 619 nm (Supplementary Fig. 1). A 633 nm dichroic mirror and 647 nm
726 long-pass emission filter were used beneath the objective lens turret to exclude
727 illumination light from the fluorescence images. The sample was illuminated with
728 narrowfield excitation of 12 μm FWHM and an intensity of 2,300 $\text{W}\cdot\text{cm}^{-2}$. Images
729 were recorded on an EMCCD camera (860 iXon+, Andor Technology Ltd) cooled to -
730 80°C. 128x128 pixel images were acquired with 1.98 ms exposure times and 128 x 29
731 pixel image strips were acquired with 0.59 ms exposure times, both for 1,000 frames
732 at the full EM and pre-amplifier gains of 300 and 4.6 respectively.

733

734 **Particle Tracking and calculation of diffusion coefficients**

735

736 All image data were recorded into .tiff files and analyzed in bespoke Matlab software.
737 Single fluorescent molecules were identified and processed into super-resolution
738 tracks using ADEMS code (Miller et al., 2015). The microscopic diffusion coefficient
739 was calculated for each tracked particle from the gradient of a linear relation fitted to
740 a plot of the mean square displacements against the four different step time intervals
741 that can be calculated from the first four steps in a track. The microscopic diffusion
742 coefficient distributions comprised an immobile fraction that had non-specifically
743 adhered to the plasma-cleaned coverslip and a diffusive fraction. Microscopic
744 diffusion coefficients were binned into histograms with bin width given by the
745 localization precision of the immobilized (heparan sulfate) data. The probability
746 distribution of diffusion coefficients was modeled by a gamma distribution (Qian et
747 al., 1991; Saxton, 1997; Vrljic et al., 2002; Zawadzki et al., 2015):

748

$$F(x, D, N) = \frac{\left(\frac{N}{D}\right)^N x^{N-1} e^{-\frac{Nx}{D}}}{(N-1)!}$$

749

750

751 where N is the number of independent steps in a track and D is the true diffusion
752 coefficient. The histogram data was fitted iteratively with a two-gamma distribution to
753 account for the mobile and immobile fractions. Initial fitting constraints conserved
754 the number of tracks and assumed the number of independent steps in a track was 4 or
755 less, giving a first estimation of the diffusion coefficients. Then fluorescence
756 microscopy data with the found diffusion coefficients was simulated with and without
757 noise, tracked, and the distribution of diffusion coefficients was fitted with the same
758 constraints as the actual data. Fitting parameters were refined based on the results of
759 fitting to the simulated data, and the experimental data was fitted with the refined
760 constraints. The process of simulating the data, fitting the simulation to refine the
761 constraints and fitting the experimental data was repeated until the simulation
762 represented the experimental data and the fit to the simulation data converged to the
763 diffusion coefficient values simulated.

764

765 For immobilized spots the N value was less than 1, implying that the steps are not
766 independent. This is expected for immobile molecules as the localization precision
767 uncertainty is larger than the diffusion distance. For mobile spots N was fixed at two
768 as there are two steps that do not contain any common localizations when only the
769 first four steps of a track are used.

770

771 **Simulation of fluorescence microscopy data.**

772

773 Image datasets were simulated in bespoke MATLAB software at given diffusion
774 coefficients using foci intensity, foci spot width, background intensity and foci
775 density data from real images. Foci are created at random locations in the image
776 frame with intensity randomly chosen from a localization in an experimental dataset.
777 The new positions of a focus in the x and y directions after initial generation are each
778 determined from a Gaussian distribution centered on the previous spot location with a
779 standard deviation of the mean square displacement of a particle in one direction, $2Dt$,
780 where D is the simulated diffusion coefficient and t is the time interval between
781 frames. To incorporate photobleaching and other effects causing truncation of
782 trajectories foci were randomly reassigned to a new location 10% of the time,
783 however diffusion within a frame was not explicitly incorporated into the model
784 beyond the use of the spot width of real localisations. The resulting image stack was
785 used for no-noise simulations. Readout noise in the detector was incorporated in the
786 simulations by the addition of zero mean Gaussian white noise, the intensity of which
787 depended on the local intensity. For tissue data simulation the mean background level
788 and standard deviation of the noise were taken from control data, away from
789 autofluorescent ECM.

790

791 **Bootstrapping**

792

793 Errors on the found values of the diffusion coefficients from FRAP, FCS and single
794 molecule tracking were found by bootstrapping (Asbury et al., 2003; Efron and
795 Tibshirani, 1994). In this method, a randomly chosen 80% of the data is fitted in the
796 same way as the entire data set and the standard deviation on each parameter from ten
797 repeats of this process is taken as the error on each fit parameter found from 100% of
798 the data.

799

800 **Single molecule imaging in tissue sections**

801

802 Tissue sections were stained with a FITC-conjugated antibody that binds B220 (RA3-
803 6B2, purchased from eBioscience). Tissue sections were subsequently imaged at low
804 (1.2 $\mu\text{m}/\text{pixel}$) magnification with green illumination (wavelength 470 nm
805 (Supplementary Fig. 1), 12 μm FWHM, intensity of 875 $\text{W}\cdot\text{cm}^{-2}$) to determine the
806 location of the B cell follicles, before switching to high (120 nm/pixel) magnification
807 and red illumination to image chemokines in these areas.

808

809 **Segmentation of tissue sections images**

810

811 Image acquisitions in tissue contain regions of autofluorescent ECM (see
812 Supplementary Note and Supplementary Fig. 5) which are identified by the tracking
813 software. These images must be segmented to identify tracks due to fluorescently
814 labeled chemokine or ECM. Intensity averages of the image acquisition were top hat
815 filtered with a structuring element of radius 4 pixels. The resulting image was
816 converted to binary form using a threshold defined by Otsu's method and the binary
817 image used to enhance the extracellular matrix regions of the original image. Small
818 holes in the thresholded region were filled by sequential erosion and dilation with a
819 disk of radius 2 pixels as the structuring element.

820

821 **Code availability**

822

823 All our bespoke software developed is freely and openly accessible via
824 <https://sourceforge.net/projects/york-biophysics/>

825

826 **Statistics**

827 Goodness-of-fit values for modeling of the distribution of microscopic diffusion
828 coefficients were evaluated using χ^2 tests as detailed in the text. Experimentally
829 measured stoichiometry distributions were compared against random overlap
830 predictions in a pairwise fashion where appropriate using Pearson's χ^2 test.

831

832 **Acknowledgments**

833

834 Supported by the Biological Physical Sciences Institute (BPSI), MRC grants
835 MR/K01580X/1 (P.O.T. and M.C.L.), MC_PC_15073 (M.C.C. and M.C.L.) and
836 BBSRC grant BB/N006453/1 (A.J.M.W. and M.C.L.). J.C. is supported by a
837 studentship from the Wellcome Trust 4-year PhD programme (WT095024MA):
838 Combating Infectious Disease: Computational Approaches in Translation Science.
839 The authors thank Jo Marrison and Andrew Leech (Bioscience Technology Facility,
840 University of York) for technical assistance with FCS and FRAP microscopy, and for
841 SEC-MALLs respectively, Chris Power (Carl Zeiss Microscopy) for help with FCS,
842 and Anne Theury for providing lymph node tissue sections.

843

844 **Author Contributions**

845 H.M. built the bespoke fluorescence microscope, overseen by M.C.L.; J.C. prepared
846 biological samples overseen by M.C.C. H.M. and J.C. performed the imaging except
847 the confocal microscopy showing binding specificity of CXCL13-AF647 performed
848 and analyzed by E.T. and Z.Z. A.W. performed the overlap calculations. H.M.
849 analyzed all other data with input from A.W., M.C.L.. H.M. ran simulations of

850 fluorescence data on code adapted from A.W.. P.O.T. oversaw FCS and FRAP
851 microscopy. H.M., A.W., E.T. prepared the figures with input from all authors. H.M.,
852 J.C., and M.C.L. wrote the manuscript with input from all authors.

853

854 **Competing financial interests**

855 The authors declare no competing financial interests.

856

857

858 **References**

- 859 Adkins, E. M., Samuvel, D. J., Fog, J. U., Eriksen, J., Jayanthi, L. D., Vaegter, C. B.,
860 et al. (2007). Membrane Mobility and Microdomain Association of the
861 Dopamine Transporter Studied with Fluorescence Correlation Spectroscopy and
862 Fluorescence Recovery after Photobleaching. *Biochemistry* 46, 10484–97.
863 doi:10.1021/BI700429Z.
- 864 Andrecka, J., Ortega Arroyo, J., Takagi, Y., de Wit, G., Fineberg, A., MacKinnon, L.,
865 et al. (2015). Structural dynamics of myosin 5 during processive motion revealed
866 by interferometric scattering microscopy. *Elife* 4, 393–414.
867 doi:10.7554/eLife.05413.
- 868 Asbury, C. L., Fehr, A. N., and Block, S. M. (2003). Kinesin Moves by an
869 Asymmetric Hand-Over-Hand Mechanism. *Science* (80-.). 302.
- 870 Ashley, T. T., Gan, E. L., Pan, J., and Andersson, S. B. (2016). Tracking single
871 fluorescent particles in three dimensions via extremum seeking. *Biomed. Opt.*
872 *Express* 7, 3355–3376. doi:10.1364/BOE.7.003355.
- 873 Axelrod, D., Koppel, D. E., Schlessinger, J., Elson, E., and Webb, W. W. (1976a).
874 Mobility measurement by analysis of fluorescence photobleaching recovery
875 kinetics. *Biophys. J.* 16, 1055–1069. doi:10.1016/S0006-3495(76)85755-4.
- 876 Axelrod, D., Ravdin, P., Koppel, D. E., Schlessinger, J., Webb, W. W., Elson, E. L.,
877 et al. (1976b). Lateral motion of fluorescently labeled acetylcholine receptors in
878 membranes of developing muscle fibers. *Proc. Natl. Acad. Sci. U. S. A.* 73,
879 4594–8..
- 880 Axelsson, I. (1978). Characterization of proteins and other macromolecules by
881 agarose gel chromatography. *J. Chromatogr. A* 152, 21–32. doi:10.1016/S0021-
882 9673(00)85330-3.
- 883 Balzarotti, F., Eilers, Y., Gwosch, K. C., Gynnå, A. H., Westphal, V., Stefani, F. D.,
884 et al. (2017). Nanometer resolution imaging and tracking of fluorescent
885 molecules with minimal photon fluxes. *Science* (80-.). 355, 606–612.
- 886 Barnes, A. L., Genever, P. G., Rimmer, S., and Coles, M. C. (2016). Collagen–Poly(
887 N -isopropylacrylamide) Hydrogels with Tunable Properties. *Biomacromolecules*
888 17, 723–734. doi:10.1021/acs.biomac.5b01251.
- 889 Bennett, L. D., Fox, J. M., and Signoret, N. (2011). Mechanisms regulating
890 chemokine receptor activity. *Immunology* 134, 246–256. doi:10.1111/j.1365-
891 2567.2011.03485.x.
- 892 Betzig, E., Patterson, G. H., Sougrat, R., Lindwasser, O. W., Olenych, S., Bonifacino,
893 J. S., et al. (2006). Imaging intracellular fluorescent proteins at nanometer
894 resolution. *Science* 313, 1642–5. doi:10.1126/science.1127344.
- 895 Buckley, C. D., Barone, F., Nayar, S., Bénézéch, C., and Caamaño, J. (2015). Stromal
896 Cells in Chronic Inflammation and Tertiary Lymphoid Organ Formation. *Annu.*
897 *Rev. Immunol.* 33, 715–745. doi:10.1146/annurev-immunol-032713-120252.
- 898 Calizo, R. C., and Scarlata, S. (2013). Discrepancy between fluorescence correlation
899 spectroscopy and fluorescence recovery after photobleaching diffusion

900 measurements of G-protein-coupled receptors. *Anal. Biochem.* 440, 40–48.
901 doi:10.1016/j.ab.2013.04.033.

902 Chen, X., Nadiarynkh, O., Plotnikov, S., and Campagnola, P. J. (2012). Second
903 harmonic generation microscopy for quantitative analysis of collagen fibrillar
904 structure. *Nat. Protoc.* 7, 654–669. doi:10.1038/nprot.2012.009.

905 Colditz, I. G., Schneider, M. A., Pruenster, M., and Rot, A. (2007). Chemokines at
906 large: in-vivo mechanisms of their transport, presentation and clearance. *Thromb.*
907 *Haemost.* 97, 688–693.

908 Cox, G., Kable, E., Jones, A., Fraser, I., Manconi, F., and Gorrell, M. D. (2003). 3-
909 Dimensional imaging of collagen using second harmonic generation. *J. Struct.*
910 *Biol.* 141, 53–62. doi:10.1016/S1047-8477(02)00576-2.

911 Drayton, D. L., Liao, S., Mounzer, R. H., and Ruddle, N. H. (2006). Lymphoid organ
912 development: from ontogeny to neogenesis. *Nat. Immunol.* 7, 344–353.
913 doi:10.1038/ni1330.

914 Dustin, M. L., and Baldari, C. T. (2017). “The Immune Synapse: Past, Present, and
915 Future,” in *Methods in molecular biology (Clifton, N.J.)*, 1–5. doi:10.1007/978-
916 1-4939-6881-7_1.

917 Edidin, M., Zagyansky, Y., and Lardner, T. (1976). Measurement of membrane
918 protein lateral diffusion in single cells. *Science (80-)*. 191, 466–468.

919 Efron, B., and Tibshirani, R. (1994). *An introduction to the bootstrap*. Chapman &
920 Hall

921 Ehrenberg, M., and Rigler, R. (1974). Rotational brownian motion and fluorescence
922 intensity fluctuations. *Chem. Phys.* 4, 390–401. doi:10.1016/0301-
923 0104(74)85005-6.

924 Einstein, A. (1905). Über die von der molekularkinetischen Theorie der Wärme
925 geforderte Bewegung von in ruhenden Flüssigkeiten suspendierten Teilchen.
926 *Ann. Phys.* 322, 549–560. doi:10.1002/andp.19053220806.

927 Elowitz, M. B., Surette, M. G., Wolf, P. E., Stock, J. B., and Leibler, S. (1999).
928 Protein mobility in the cytoplasm of Escherichia coli. *J. Bacteriol.* 181, 197–203.

929 Fischer, H., Polikarpov, I., and Craievich, A. F. (2004). Average protein density is a
930 molecular-weight-dependent function. *Protein Sci.* 13, 2825–8.
931 doi:10.1110/ps.04688204.

932 Fujiwara, T., Ritchie, K., Murakoshi, H., Jacobson, K., and Kusumi, A. (2002).
933 Phospholipids undergo hop diffusion in compartmentalized cell membrane. *J.*
934 *Cell Biol.* 157, 1071–81. doi:10.1083/jcb.200202050.

935 Guo, L., Har, J. Y., Sankaran, J., Hong, Y., Kannan, B., and Wohland, T. (2008).
936 Molecular Diffusion Measurement in Lipid Bilayers over Wide Concentration
937 Ranges: A Comparative Study. *ChemPhysChem* 9, 721–728.
938 doi:10.1002/cphc.200700611.

939 Gustafsson, M. G. (2000). Surpassing the lateral resolution limit by a factor of two
940 using structured illumination microscopy. *J. Microsc.* 198, 82–7.

941 Happel, J., and Brenner, H. (1981). *Low Reynolds number hydrodynamics : with*
942 *special applications to particulate media*. Springer Netherlands

943 Hell, S. W., and Wichmann, J. (1994). Breaking the diffraction resolution limit by
944 stimulated emission: stimulated-emission-depletion fluorescence microscopy.
945 *Opt. Lett.* 19, 780–2.

946 Hiramoto-Yamaki, N., Tanaka, K. A. K., Suzuki, K. G. N., Hirose, K. M.,
947 Miyahara, M. S. H., Kalay, Z., et al. (2014). Ultrafast Diffusion of a Fluorescent
948 Cholesterol Analog in Compartmentalized Plasma Membranes. *Traffic* 15, 583–
949 612. doi:10.1111/tra.12163.

950 Ikeda, S., and Nishinari, K. (2000). Intermolecular Forces in Bovine Serum Albumin
951 Solutions Exhibiting Solidlike Mechanical Behaviors. *Biomacromolecules* 1,
952 757–763. doi:10.1021/BM005587O.

953 Juette, M. F., and Bewersdorf, J. (2010). Three-Dimensional Tracking of Single
954 Fluorescent Particles with Submillisecond Temporal Resolution. *Nano Lett.* 10,
955 4657–4663. doi:10.1021/nl1028792.

956 Kienle, K., and Lämmermann, T. (2016). Neutrophil swarming: an essential process
957 of the neutrophil tissue response. *Immunol. Rev.* 273, 76–93.
958 doi:10.1111/imr.12458.

959 Lagerholm, B. C., Andrade, D. M., Clausen, M. P., and Eggeling, C. (2017).
960 Convergence of lateral dynamic measurements in the plasma membrane of live
961 cells from single particle tracking and STED-FCS. *J. Phys. D. Appl. Phys.* 50,
962 63001.

963 Leake, M. C. (2013). The physics of life: one molecule at a time. *Philos. Trans. R.*
964 *Soc. Lond. B. Biol. Sci.* 368, 20120248. doi:10.1098/rstb.2012.0248.

965 Llorente-Garcia, I., Lenn, T., Erhardt, H., Harriman, O. L., Liu, L.-N., Robson, A., et
966 al. (2014). Single-molecule in vivo imaging of bacterial respiratory complexes
967 indicates delocalized oxidative phosphorylation. *Biochim. Biophys. Acta* 1837,
968 811–24. doi:10.1016/j.bbabi.2014.01.020.

969 Machañ, R., Foo, Y. H., and Wohland, T. (2016). On the Equivalence of FCS and
970 FRAP: Simultaneous Lipid Membrane Measurements. *Biophys. J.* 111, 152–161.
971 doi:10.1016/j.bpj.2016.06.001.

972 Magde, D., Elson, E., and Webb, W. W. (1972). Thermodynamic Fluctuations in a
973 Reacting System—Measurement by Fluorescence Correlation Spectroscopy.
974 *Phys. Rev. Lett.* 29, 705–708. doi:10.1103/PhysRevLett.29.705.

975 Miller, H., Zhou, Z., Shepherd, J., Wollman, A. J. M., and Leake, M. C. (2018).
976 Single-molecule techniques in biophysics: a review of the progress in methods
977 and applications. *Reports Prog. Phys.* 81, 24601. doi:10.1088/1361-6633/aa8a02.

978 Miller, H., Zhou, Z., Wollman, A. J. M., and Leake, M. C. (2015). Superresolution
979 imaging of single DNA molecules using stochastic photoblinking of minor
980 groove and intercalating dyes. *Methods* 88, 81–88.
981 doi:10.1016/j.ymeth.2015.01.010.

982 Monneau, Y. R., Luo, L., Sankaranarayanan, N. V., Nagarajan, B., Vivès, R. R.,
983 Baleux, F., et al. (2017). Solution structure of CXCL13 and heparan sulfate
984 binding show that GAG binding site and cellular signalling rely on distinct
985 domains. *Open Biol.* 7, 170133. doi:10.1098/rsob.170133.

986 Mullineaux, C. W., Nenninger, A., Ray, N., and Robinson, C. (2006). Diffusion of
987 green fluorescent protein in three cell environments in *Escherichia coli*. *J.*
988 *Bacteriol.* 188, 3442–8. doi:10.1128/JB.188.10.3442-3448.2006.

989 Pereira, J. P., Kelly, L. M., and Cyster, J. G. (2010). Finding the right niche: B-cell
990 migration in the early phases of T-dependent antibody responses. *Int. Immunol.*
991 22, 413–9. doi:10.1093/intimm/dxq047.

992 Piliarik, M., and Sandoghdar, V. (2014). Direct optical sensing of single unlabelled
993 proteins and super-resolution imaging of their binding sites. *Nat. Commun.* 5.
994 doi:10.1038/ncomms5495.

995 Plank, M., Wadhams, G. H., and Leake, M. C. (2009). Millisecond timescale slimfield
996 imaging and automated quantification of single fluorescent protein molecules for
997 use in probing complex biological processes. *Integr. Biol.* 1, 602–12.
998 doi:10.1039/b907837a.

999 Putnam, F. (1975). *The Plasma Proteins : Structure, Function, and Genetic Control.*

1000 Second. Academic Press, New York.

1001 Qian, H., Sheetz, M. P., and Elson, E. L. (1991). Single particle tracking. Analysis of
1002 diffusion and flow in two-dimensional systems. *Biophys. J.* 60, 910–21.
1003 doi:10.1016/S0006-3495(91)82125-7.

1004 Rashid, R., Chee, S. M. L., Raghunath, M., and Wohland, T. (2015). Macromolecular
1005 crowding gives rise to microviscosity, anomalous diffusion and accelerated actin
1006 polymerization. *Phys. Biol.* 12, 34001. doi:10.1088/1478-3975/12/3/034001.

1007 Reyes-Lamothe, R., Sherratt, D. J., and Leake, M. C. (2010). Stoichiometry and
1008 architecture of active DNA replication machinery in *Escherichia coli*. *Science*
1009 328, 498–501. doi:10.1126/science.1185757.

1010 Robson, A., Burrage, K., and Leake, M. C. (2013). Inferring diffusion in single live
1011 cells at the single-molecule level. *Philos. Trans. R. Soc. Lond. B. Biol. Sci.* 368,
1012 20120029. doi:10.1098/rstb.2012.0029.

1013 Rot, A., and von Andrian, U. H. (2004). Chemokines in innate and adaptive host
1014 defense: basic chemokines grammar for immune cells. *Annu. Rev. Immunol.* 22,
1015 891–928. doi:10.1146/annurev.immunol.22.012703.104543.

1016 Rust, M. J., Bates, M., and Zhuang, X. (2006). Sub-diffraction-limit imaging by
1017 stochastic optical reconstruction microscopy (STORM). *Nature* 3, 793–795.
1018 doi:10.1038/NMETH929.

1019 Saxton, M. J. (1997). Single-particle tracking: the distribution of diffusion
1020 coefficients. *Biophys. J.* 72, 1744–1753. doi:10.1016/S0006-3495(97)78820-9.

1021 Schneider, J., Zahn, J., Maglione, M., Sigrist, S. J., Marquard, J., Chojnacki, J., et al.
1022 (2015). Ultrafast, temporally stochastic STED nanoscopy of millisecond
1023 dynamics. *Nat. Methods* 12, 827–30. doi:10.1038/nmeth.3481.

1024 Schulz, O., Hammerschmidt, S. I., Moschovakis, G. L., and Förster, R. (2016).
1025 Chemokines and Chemokine Receptors in Lymphoid Tissue Dynamics. *Annu.*
1026 *Rev. Immunol.* 34, 203–242. doi:10.1146/annurev-immunol-041015-055649.

1027 Simon Davis, D. A., and Parish, C. R. (2013). Heparan sulfate: a ubiquitous
1028 glycosaminoglycan with multiple roles in immunity. *Front. Immunol.* 4, 470.
1029 doi:10.3389/fimmu.2013.00470.

1030 Song, L., Lu-Walther, H.-W., Förster, R., Jost, A., Kielhorn, M., Zhou, J., et al.
1031 (2016). Fast structured illumination microscopy using rolling shutter cameras.
1032 *Meas. Sci. Technol.* 27, 55401. doi:10.1088/0957-0233/27/5/055401.

1033 van 't Hoff, M., de Sars, V., and Oheim, M. (2008). A programmable light engine for
1034 quantitative single molecule TIRF and HILO imaging. *Opt. Express* 16, 18495.
1035 doi:10.1364/OE.16.018495.

1036 von Hundelshausen, P., Agten, S. M., Eckardt, V., Blanchet, X., Schmitt, M. M.,
1037 Ippel, H., et al. (2017). Chemokine interactome mapping enables tailored
1038 intervention in acute and chronic inflammation. *Sci. Transl. Med.* 9.

1039 Vrljic, M., Nishimura, S. Y., Brasselet, S., Moerner, W. E., and McConnell, H. M.
1040 (2002). Translational diffusion of individual class II MHC membrane proteins in
1041 cells. *Biophys. J.* 83, 2681–92. doi:10.1016/S0006-3495(02)75277-6.

1042 Wieser, S., Moertelmaier, M., Fuertbauer, E., Stockinger, H., and Schütz, G. J.
1043 (2007). (Un)confined diffusion of CD59 in the plasma membrane determined by
1044 high-resolution single molecule microscopy. *Biophys. J.* 92, 3719–28.
1045 doi:10.1529/biophysj.106.095398.

1046 Wollman, A. J., Shashkova, S., Hedlund, E. G., Friemann, R., Hohmann, S., and
1047 Leake, M. C. (2017). Transcription factor clusters regulate genes in eukaryotic
1048 cells. *Elife* 6. doi:10.7554/eLife.27451.

1049 Zawadzki, P., Stracy, M., Ginda, K., Zawadzka, K., Lesterlin, C., Kapanidis, A. N., et

1050
1051
1052
1053

al. (2015). The Localization and Action of Topoisomerase IV in Escherichia coli Chromosome Segregation Is Coordinated by the SMC Complex, MukBEF. *Cell Rep.* 13, 2587–96. doi:10.1016/j.celrep.2015.11.034.

In review

1054
1055
1056
1057
1058
1059
1060
1061
1062
1063
1064
1065
1066
1067
1068
1069
1070
1071
1072
1073
1074
1075
1076
1077
1078
1079
1080
1081
1082
1083
1084
1085
1086
1087
1088
1089
1090
1091
1092
1093
1094
1095
1096
1097
1098
1099
1100
1101
1102
1103

Figure 1 Schematic diagrams of high-speed narrowfield microscopy and the experimental system. (a) The imaging framework showing the bespoke fluorescence microscope and diagrams of image acquisition. (b) The structure of AF647 labeled CCL19 and CXCL13.

Figure 2 Single-molecule stoichiometry of CCL19-AF647. (a) Tracking of photoblinking AF647: localizations and intensity over time with sample images from the acquisition. (b) Distribution of apparent CCL19 foci stoichiometry (grey) overlaid with the predicted distribution based on randomly overlapping PSFs (blue). (c) Kernel density estimates of intensity of AF647 labeled CCL19 in collagen (solid blue line), and under heparan sulfate immobilization (solid black line); CXCL13 in collagen (dotted blue line), and under heparan sulfate immobilization (dotted black line); and BSA in 10% Ficoll (solid red line). All traces are normalized to the primary peak for clarity (see Supplementary Material).

1104
1105
1106
1107
1108
1109
1110
1111
1112
1113
1114
1115
1116
1117
1118
1119
1120
1121
1122
1123
1124
1125
1126
1127
1128
1129
1130
1131
1132
1133
1134
1135
1136
1137
1138
1139
1140
1141
1142
1143
1144
1145
1146
1147
1148

Figure 3 Simulations of chemokine data. (a) Sample simulation images, shown with and without Gaussian white noise added. Scale bar 1 μm . (b) Two-gamma distribution fit (red) to diffusion coefficients found from a simulation of 1.6 and 10 $\mu\text{m}^2\text{s}^{-1}$ data with Gaussian white noise. (c) Histograms showing the distribution of simulated 0 $\mu\text{m}^2\text{s}^{-1}$ data with (red, overlaid) and without (blue) Gaussian white noise. (d) Diffusion coefficient distribution from a simulation of 0 and 9 $\mu\text{m}^2\text{s}^{-1}$ data with Gaussian white noise. Fitted populations are shown in black for the immobile, red for the mobile and blue for the combined fit. Shaded areas indicate one standard deviation.

In review

1149 **Figure 4 Comparing FRAP, FCS, and single molecule tracking on BSA-AF647 in**
1150 **10% Ficoll 400.** (a) Single-molecule tracking: Simplified schematic of the stages in
1151 tracking and the resulting fit with shaded regions indicating error bounds of one
1152 standard deviation. (b) FRAP: schematic of technique, profile of bleached region in an
1153 immobilized sample and example fluorescence intensity recovery trace. (c) FCS:

1154 Schematic of the confocal volume, example section of intensity fluctuation trace and
1155 correlation curve.

1156
1157
1158
1159
1160
1161
1162
1163
1164
1165
1166
1167
1168
1169
1170
1171

1172 **Figure 5 Single particle tracking of chemokines in collagen.** SHIM of collagen
1173 network in (a) 2D and (b) 3D. (c) Representative consecutive sub-millisecond images
1174 of chemokines in collagen. (d), (e) Fitted diffusion coefficient distribution of
1175 CXCL13-AF647 and CCL19-AF647 showing mobile and immobile components in a
1176 collagen matrix with (f) just the fitted high mobility diffusion coefficient distributions
1177 of CXCL13-AF647 (cyan) and CCL19-AF647 (magenta) (shaded areas indicate one
1178 standard deviation).

1179
1180
1181
1182
1183
1184
1185
1186
1187
1188
1189
1190
1191

1192 **Figure 6 Confocal microscopy quantification of CXCL13-AF647 binding to**
1193 **lymph node follicles.** (a) Schematic diagram of approximate locations of B cell
1194 follicles in a wild type murine lymph node. (b) Exemplar confocal microscopy images
1195 of CXCL13-AF647 and BSA-AF647 binding to lymph node tissue follicles (B220+
1196 regions of lymph node tissue sections), and control with only B220 staining. (c)
1197 Quantification of the total fluorescent intensity for a fixed size imaging plane within a
1198 lymph node follicle. Each data point represents a distinct follicle.

1199

1200
1201
1202
1203
1204
1205
1206
1207
1208
1209
1210
1211
1212
1213
1214
1215
1216
1217
1218
1219
1220
1221
1222
1223
1224
1225
1226
1227
1228
1229
1230
1231
1232
1233
1234
1235
1236
1237
1238
1239
1240
1241
1242
1243
1244
1245
1246
1247
1248
1249

Figure 7 Single molecule analysis of CXCL13-AF647 in tissue. (a) Intensity average image of image acquisition to show autofluorescent ECM in B220 stained B cell follicle with no added chemokine. (b) Areas of (a) identified as ECM by segmentation with overlaid track localizations colored orange. (c) Intensity average image of image acquisition to show autofluorescent ECM in B220 stained B cell follicle with added chemokine. (d) Areas of (c) identified as ECM by segmentation with overlaid track localizations colored by location on ECM (blue) or in the interstitial spaces between cells (cyan). (e) Comparison of diffusion coefficients of localisations in ECM locations in the presence (blue) and absence (orange) of CXCL13-AF647 (f) Comparison of diffusion coefficients for the ECM (blue) and chemokine (cyan) populations when tracking CXCL13-AF647 in lymph node tissue shown. (g) Distribution and fit of chemokine diffusion coefficients of CXCL13-AF647 in tissue sections, shaded area indicates one standard deviation.

In review

1250
1251
1252
1253
1254
1255
1256
1257
1258

Simulated condition	Number of Tracks	Fitted value of D ($\mu\text{m}^2\text{s}^{-1}$)	Fitted value of N ($\mu\text{m}^2\text{s}^{-1}$)	R^2 value of fit
$1.6 \mu\text{m}^2\text{s}^{-1}$, no noise	1,579	1.72 (1.68, 1.76)	2.24 (2.15, 2.33)	0.9892
$1.6 \mu\text{m}^2\text{s}^{-1}$, noise	401	2.19 (2.12, 2.25)	1.75 (1.67, 1.83)	0.9777
$10 \mu\text{m}^2\text{s}^{-1}$, no noise	1,519	10.21 (9.77, 10.6)	2.27 (2.08, 2.45)	0.9343
$10 \mu\text{m}^2\text{s}^{-1}$, noise	463	10.04 (9.53, 10.54)	2.77 (2.47, 3.08)	0.8968

1259 **Table 1 Results of one gamma distribution fitting to simulated single diffusion**
1260 **coefficient distributions.** Noise or no noise refers to the presence of Gaussian white
1261 noise proportional to the intensity in the simulation. 95% confidence intervals are
1262 given in brackets.

1263
1264
1265
1266
1267
1268
1269
1270
1271
1272
1273
1274
1275
1276
1277
1278
1279
1280
1281
1282
1283
1284
1285
1286
1287
1288
1289

1290
1291
1292
1293
1294
1295
1296
1297
1298
1299
1300
1301
1302
1303
1304
1305

Condition	Diffusion coefficient ($\mu\text{m}^2\text{s}^{-1}$)	Number of measurements
Theoretical with Stokes radius 3.48nm	12.3 \pm 0.1	
FCS	18.8 \pm 0.3	27 traces
FRAP	7.1 \pm 0.3	30 repeats
Single-molecule tracking	9.3 \pm 0.4	2,608 tracks (fitted 1,113 mobile tracks)

1306 **Table 2 Measurements of the diffusion coefficient of Alexa-647 labeled BSA in**
1307 **10% Ficoll 400.** Variation on the theoretical value is due to a potential $\pm 2^\circ\text{C}$
1308 temperature change in the laboratory.
1309
1310
1311
1312
1313
1314
1315
1316
1317
1318
1319
1320
1321
1322
1323
1324
1325
1326
1327
1328
1329
1330
1331

1332
1333
1334
1335
1336
1337
1338
1339

AF647 labelled chemokine	Theoretical diffusion coefficients in water ($\mu\text{m}^2\text{s}^{-1}$)	Fitted diffusion coefficient ($\mu\text{m}^2\text{s}^{-1}$)	Error ($\mu\text{m}^2\text{s}^{-1}$)	Number of highly mobile tracks	R^2 of combined fit
CXCL13	149	6.2	0.3	1,930	0.980
CCL19	146	8.4	0.2	4,859	0.984

1340
1341
1342
1343
1344
1345

Table 3 Diffusion coefficients of CXCL13 and CCL19 in collagen. Optimized values were found by fitting a two gamma distribution to single molecule tracking data.

In review

Figure 1.TIF

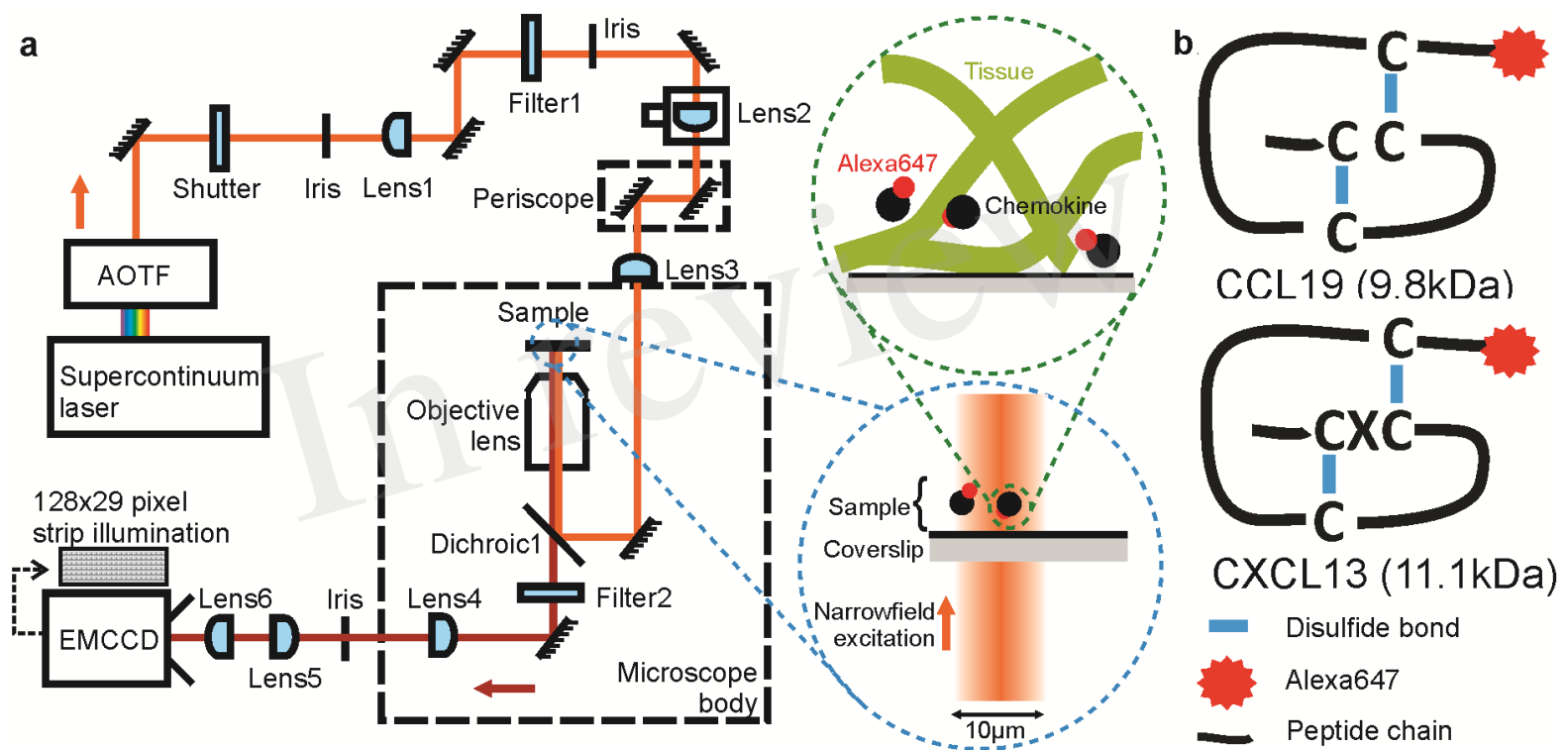


Figure 2.TIF

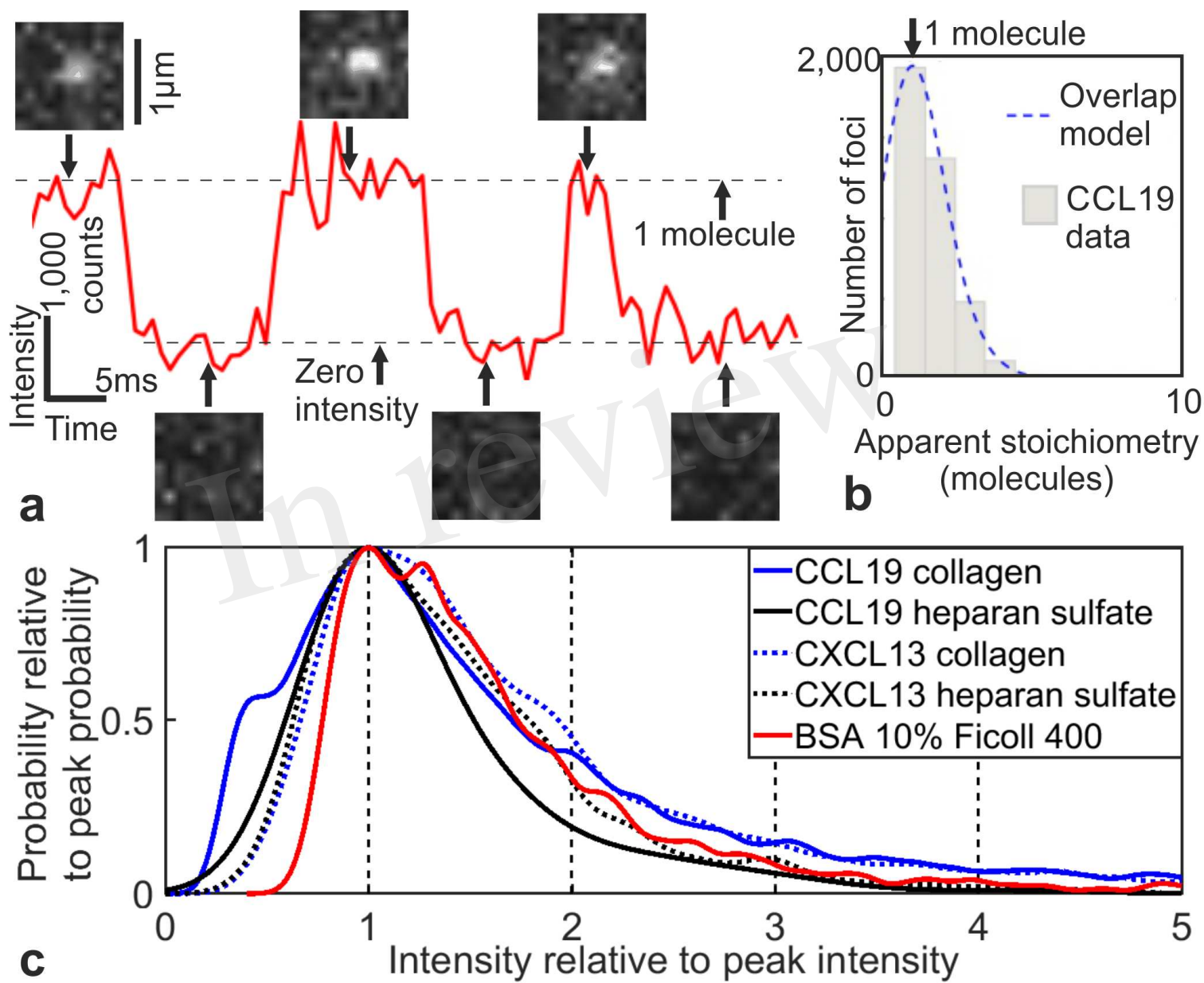


Figure 3.TIF

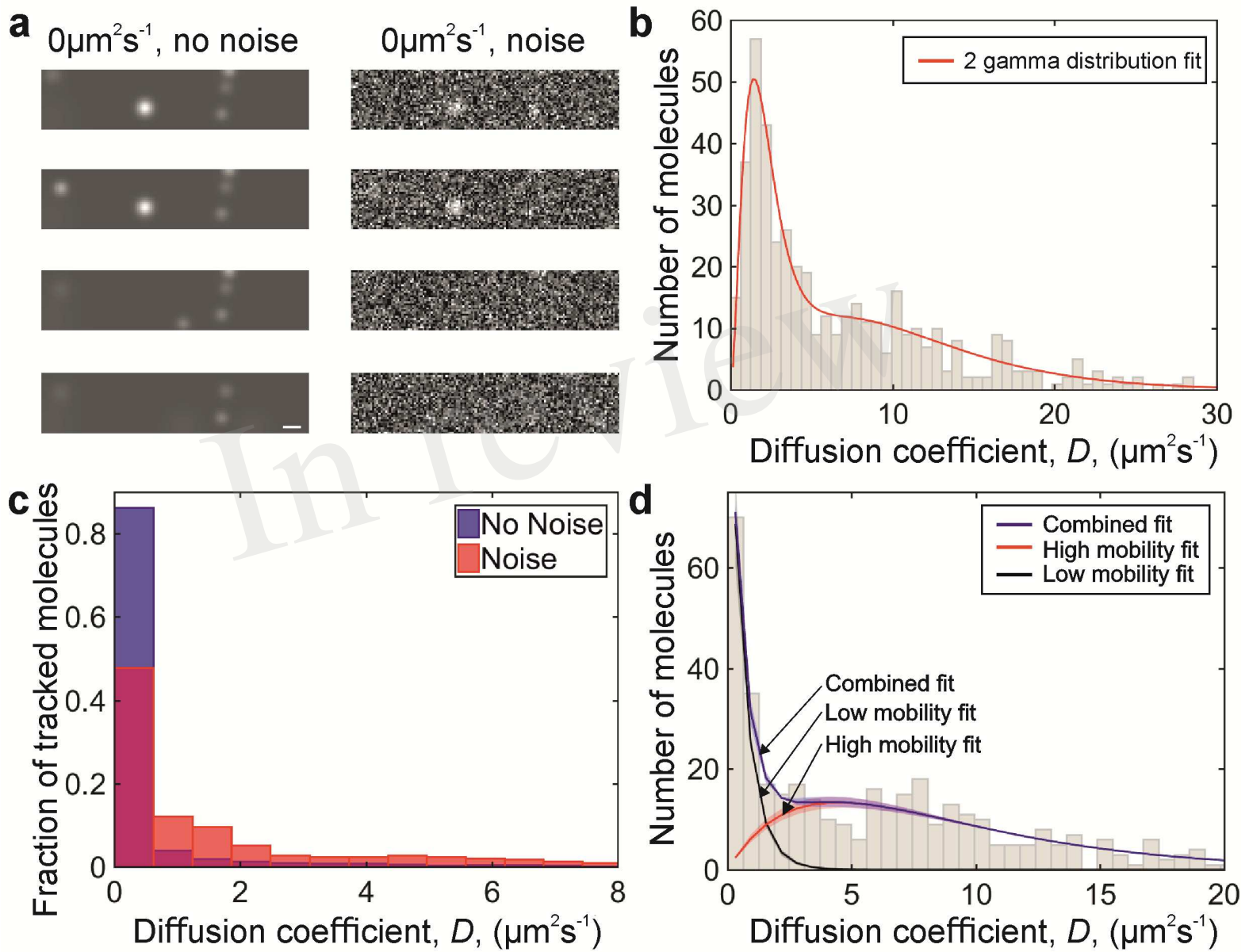


Figure 4.TIF

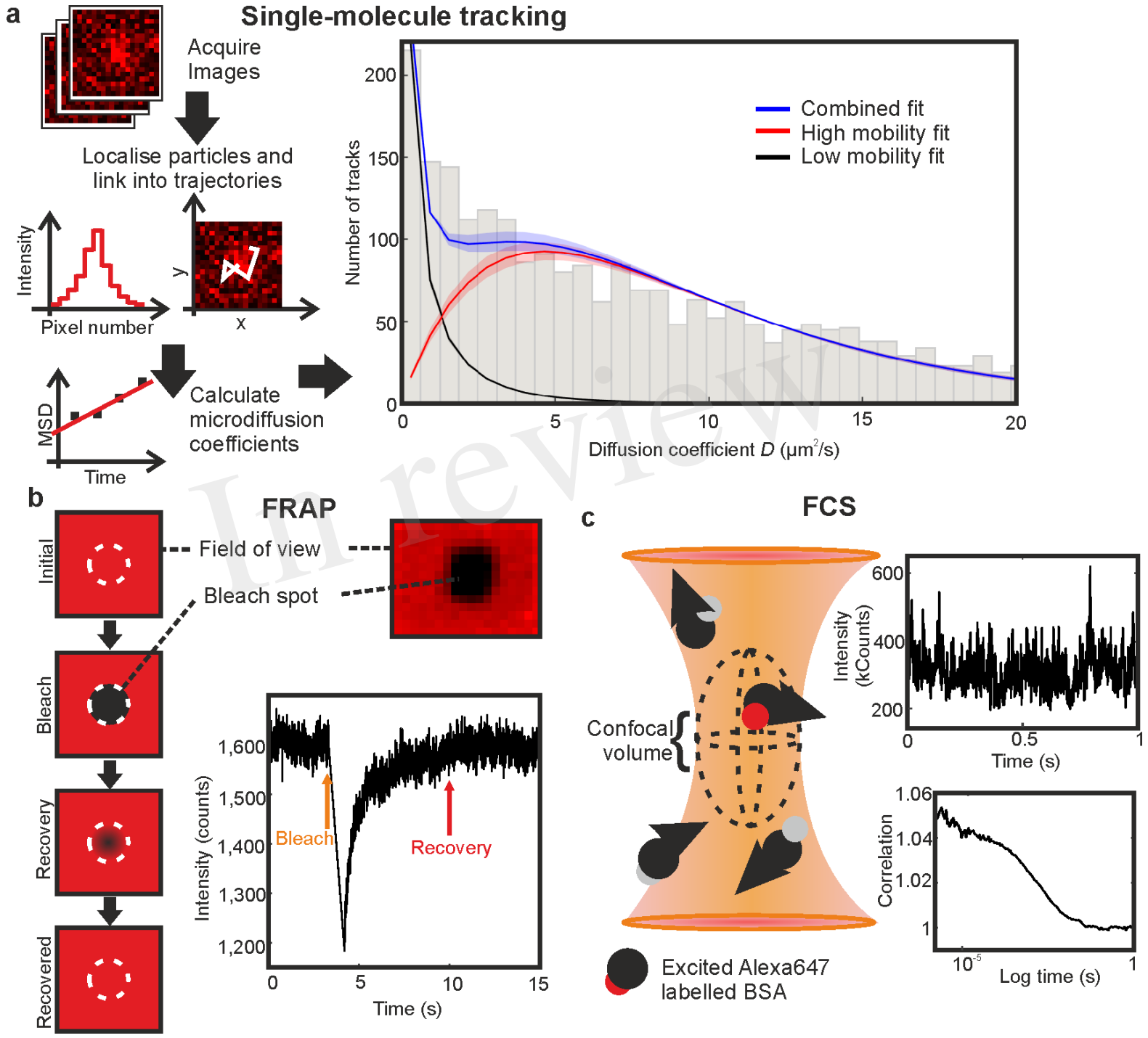


Figure 5.TIF

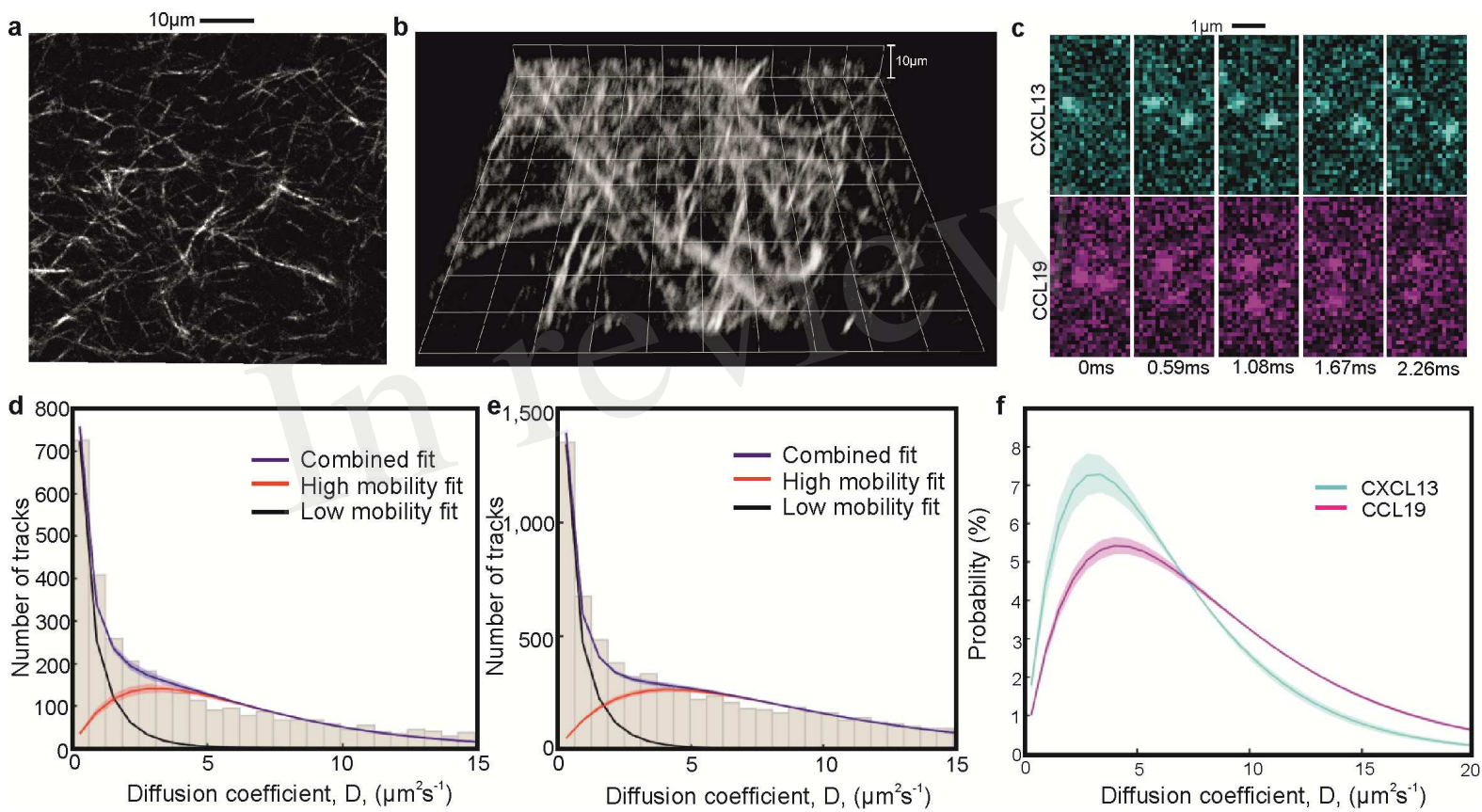


Figure 6.TIF

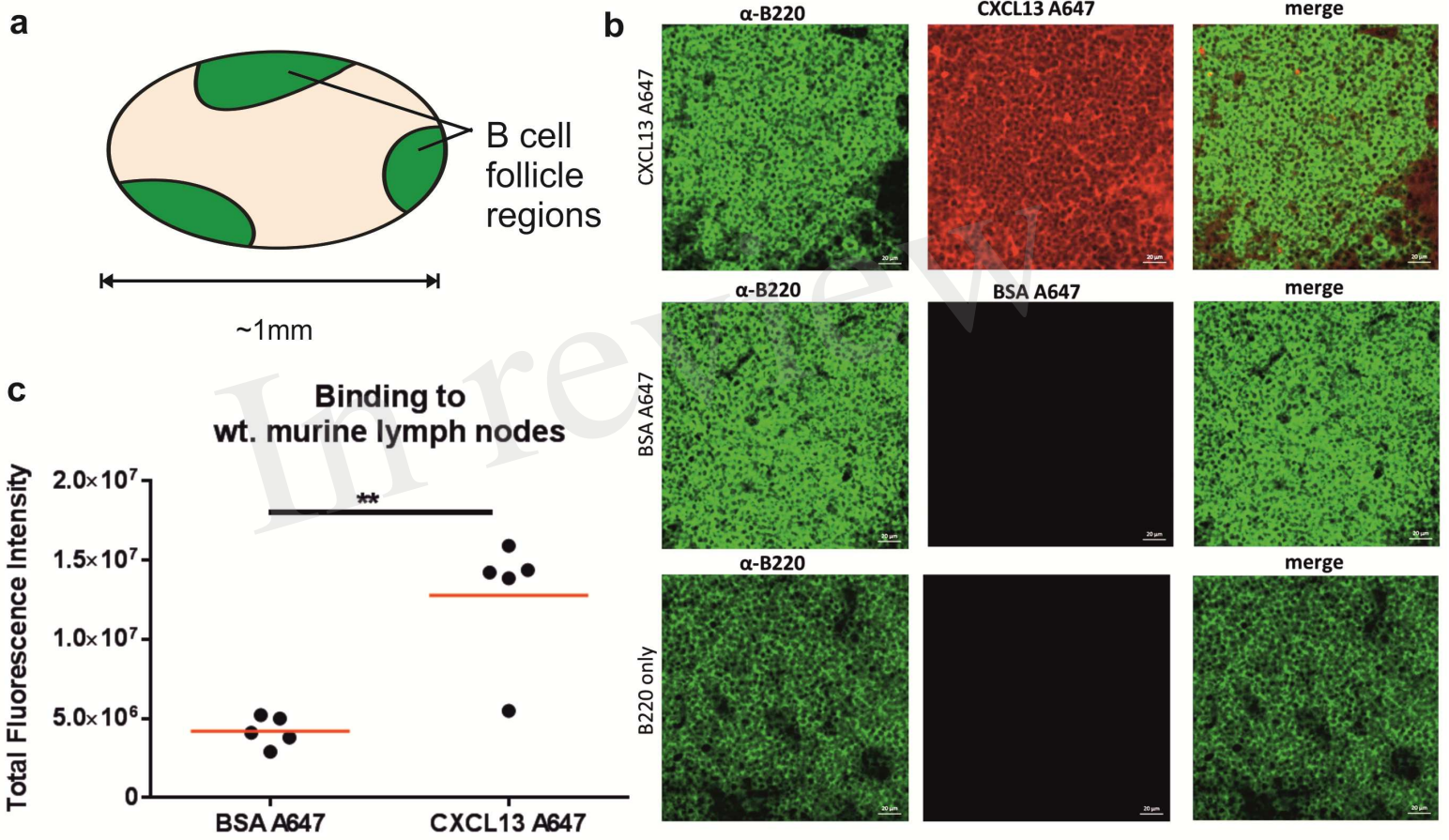


Figure 7.TIF

